

KATHRIN KLEINBACH

RYDBERG SPECTROSCOPY IN HOLLOW CORE FIBERS

MASTER THESIS

STUTT GART APRIL 2014

5. PHYSIKALISCHES INSTITUT, UNIVERSITÄT STUTT GART

Master Thesis

Rydberg Spectroscopy in Hollow Core Fibers

Kathrin Kleinbach

Stuttgart, April 2014

Examiner: Prof. Dr. Tilman Pfau
Second Examiner: Prof. Dr. Harald Giessen
Supervisor: Dr. Robert Löw

5. Physikalisches Institut
Universität Stuttgart
Pfaffenwaldring 57, 70569 Stuttgart

Abstract

In this work it is shown that thermal cesium atoms confined inside hollow core fibers can be excited to Rydberg states. Rydberg atoms with main quantum numbers between $n = 26$ and $n = 46$ were detected using a three photon excitation scheme. The experiments were performed in kagomé hollow core photonic crystal fibers with core diameters of $60\ \mu\text{m}$ and $19\ \mu\text{m}$, as well as in a capillary with a core diameter of $70\ \mu\text{m}$. A theoretical model was developed, which reproduces the line shape of the spectra obtained. In the kagomé hollow core photonic crystal fiber with $19\ \mu\text{m}$ core diameter, light induced atomic desorption was analyzed, while the beam evoking this desorption was switched. The diffusion of cesium atoms into hollow core fibers was simulated, including absorption and desorption of the atoms on the fiber walls.

Zusammenfassung

In dieser Arbeit wird gezeigt, dass es möglich ist, in Hohlkernfasern eingeschlossene thermische Zäsiumatome in Rydbergzustände anzuregen. Rydbergatome mit Hauptquantenzahlen zwischen $n = 26$ und $n = 46$ wurde mit Hilfe eines Dreiphotonenanregungsschemas angeregt und spektroskopisch nachgewiesen. Die Experimente wurden sowohl in Hohlkern-photonischen Kristallfasern mit einer Kagoméstruktur und Kerndurchmessern von $60\ \mu\text{m}$ und $19\ \mu\text{m}$ durchgeführt, als auch in Quarzkapillaren mit einem Kerndurchmesser von $70\ \mu\text{m}$. Ein theoretisches Modell welches entwickelt wurde, ist in der Lage die Linienform der gemessenen Spektren im Wesentlichen zu reproduzieren. In der Fasern mit $19\ \mu\text{m}$ Kerndurchmesser wurde analysiert, wie sich lichtinduzierte atomare Desorption ändert, wenn der Strahl ein und aus geschaltet wird, welcher die Desorption hervorruft. Die Diffusion von Zäsiumatomen in Hohlkernfasern wurde simuliert, wobei Absorption und Desorption von Atomen an den Faserwänden berücksichtigt wurde.

Contents

1	Motivation	1
2	Theoretical Background: Atomic Physics	3
2.1	Atom Light Interaction	3
2.1.1	Density Matrix Formalism	3
2.1.2	Two Level System	4
2.1.3	Absorption in a Two Level System	6
2.1.4	Absorption in a Thermal Vapor	7
2.1.5	Gaussian Beam Profile	8
2.1.6	Four Level System	8
2.2	Rydberg Atoms	10
2.3	DC Stark Effect	11
3	Theoretical Background: Hollow Core Fibers	13
3.1	Light Guidance in Capillaries	13
3.2	Kagomé Hollow Core Photonic Crystal Fibers	16
3.3	Light Induced Atomic Desorption	18
4	Experimental Setup	19
4.1	Cesium	19
4.2	Excitation Scheme and Laser Setup	20
4.3	Setup of the Three Photon Spectroscopy	23
4.4	Fibers used in the Experiment	24
4.4.1	HC-PCF with 60 μm and 19 μm core size	24
4.4.2	Capillary with 70 μm core size	26
4.5	Optical Depth in Hollow Core Fibers	27
5	Diffusion of Cesium Vapor into Fibers	29
6	Measurements on Light Induced Atomic Desorption	33
7	Rydberg Spectroscopy	37
7.1	Spectra in Kagomé HC-PCF with low Optical Depth	37
7.2	Spectra in Kagomé HC-PCF with high Optical Depth	44
7.3	Spectra in 70 μm Capillary	48
7.4	Off-resonant Rydberg Excitation	49

8 Simulation of the Four Level System	53
8.1 Model	53
8.2 Fitting the Model to the Experimental Data	56
9 Summary	59
A Numbers used in the Simulation	61
B Wavelengths for the Rydberg transition	63
C Spectra Measured in Kagomé HC-PCF	65
Bibliography	69

1 Motivation

Highly excited atoms, so-called Rydberg atoms, strongly interact with each other or their environment due to their exceptionally large polarizability. The strong interaction is reflected in a severe distortion of the energy levels, resulting in optical non-linearities when performing spectroscopy. In quantum optics [1–3], quantum computation [4–6] and quantum simulation [7] this optical non-linearities are mainly studied with cold atoms. Experiments based on thermal atoms at room temperature have recently shown that Rydberg excitation is also possible in micrometer-sized cells [8] and Rydberg-Rydberg interaction can be observed [9]. As one example for an application, Rydberg states excited in a hot vapor can be exploited for metrology [10].

The implementation of Rydberg excitation in a hot vapor provides the basics for integrating Rydberg physics into technical feasible, miniaturized devices. The invention of hollow core photonic crystal fibers [11] has opened up new possibilities to perform atomic spectroscopy inside a fiber with both hot [12–17] and cold atoms [18]. Hollow core fibers do not only provide a confinement for the atoms, but also enable to control the mode structure of the light field [19]. Additionally, the confinement of the light field allows to overcome the limitation set by the Rayleigh length and the free space diffraction limit. This could lead to an integration of Rydberg physics into fiber networks, but could also form the basis for further quantum optical experiments with a better control of the light field.

The proof that Rydberg excitation is possible close to confining surfaces [8] has been encouraging for the realization of Rydberg spectroscopy inside hollow core fibers. The theoretical potential of the system and its advantages have been proposed in [20]. However, the experimental realization still needs to be demonstrated.

In this work, the Rydberg excitation of cesium atoms confined in a hollow core fiber is reported. In the experiment presented, kagomé hollow core photonic crystal fibers (kagomé HC-PCF) were chosen, as they provide broadband transmission and are therefore ideally suited for the required multi-color excitation. In addition, kagomé HC-PCF are well suited as they have very thin core walls of about 200 nm, which could lead to reduced atom wall interaction. A large core diameter of 60 μm was chosen for the very first try and further measurements in a fiber with 19 μm core diameter were performed. To compare the effect of the thin walls to fibers with thick core walls, Rydberg spectroscopy inside a capillary was tested as well.

Cesium atoms were chosen, as the level structure of alkali atoms is less complex than for other atoms, the Rydberg excitation can be performed with infrared light and cesium has a higher vapor pressure at room temperature than other alkali metals

1 Motivation

e.g. rubidium. Additionally, there is only one stable isotope of cesium. The fibers were exposed to the cesium atmosphere up to four months. In order to excite the cesium atoms to a Rydberg state, a three photon excitation was performed. All three wavelengths are in the infrared. This experimentally gives simple access to a high coupling strength of the Rydberg transition and matches the guiding properties of the fibers.

During the work, it became clear that the light induced atomic desorption in the fiber needs to be characterized to ensure that the vapor pressure inside the fiber is stable. Additionally, the diffusion of the cesium atoms into the hollow core fibers was studied to understand the timescales for the filling process of the fibers.

2 Theoretical Background: Atomic Physics

In this work, atoms inside hollow core fibers are investigated spectroscopically. Therefore, the atom light interaction is introduced in section 2.1. Characteristics of Rydberg atoms are discussed in section 2.2. Finally, the DC Stark effect is explained, which occurs when atoms are exposed to static electric fields.

2.1 Atom Light Interaction

Pure quantum mechanical systems states are represented by a state vector in Hilbert space and the evolution of the states can be calculated using the Schrödinger equation. If however, the system contains a statistical mixture of states, it can not be described by the Schrödinger equation anymore. The density matrix formalism needs to be applied, which is introduced in section 2.1.1. Some effects, like the spontaneous decay from an energetically higher state of an electron to a lower one, are also described more easily with this formalism using the Lindblad equation.

The atom light interaction is introduced in section 2.1.2, considering a two level system, for which the absorption is derived in section 2.1.3. The theory is extended in section 2.1.4, to include the thermal motion of the atoms. In section 2.1.5, it is shown, how the Gaussian beam profile can be considered. The four level system, which is needed to describe the Rydberg spectroscopy performed in this work, is explained in section 2.1.6.

2.1.1 Density Matrix Formalism

In atomic spectroscopy, alkali atoms are often chosen because they only have one valence electron. One can assume that only the valence electron of the atom interacts with the light field and therefore, this system can then be described like a hydrogen atom. The valence electron can be in one of the energy eigenstates $|1\rangle$, $|2\rangle$ etc. of the atom or in a superposition of them. As long as one only needs to describe the atom light interaction, the Schrödinger formalism can be applied. When the spontaneous decay from an energetically higher state of the electron to a lower one is included, no hermitian Hamiltonian can be used. To apply the Lindblad equation, which is needed then, the system has formally to be described by a *density operator* ρ , which is given by

$$\rho(t) = \sum_i p_i |\psi_i(t)\rangle \langle \psi_i(t)|. \quad (2.1)$$

2 Theoretical Background: Atomic Physics

It consists of the projection operators $\langle \psi_i(t) |$ on the electronic states weighted by the probability p_i to find this state i in the mixture.

The density operator can be written as a matrix with the ground state of the atom, first excited state etc. chosen as basis. In such a matrix, the diagonal elements show the populations which are the probabilities to find the system in the corresponding states. The non-diagonal elements show the coherence between two states; when it is zero, the relation of the phases of the two states is completely unknown. The density matrix has useful mathematical properties: it is a hermitian matrix, its trace is always one and it is positive semi-definite.

When the quantum mechanical states are described by density matrices, the time evolution can be performed using the *Liouville van Neumann equation*

$$\dot{\rho} = -\frac{i}{\hbar}[H, \rho]. \quad (2.2)$$

In this equation, H is the Hamilton operator of the system, the eigenvalues of which are the energies of the corresponding quantum mechanical state. The interaction between the atom and the light field is also described by this Hamiltonian.

The description of spontaneous decay of an energetically high electronic state into a lower lying state by coupling to the environment would ask for a Hamiltonian including not only the atomic levels and the light, but all atoms around, virtual particles and more. To avoid this complexity, spontaneous decay is included into our calculations by the *Lindblad equation*

$$\dot{\rho} = -\frac{i}{\hbar}[H, \rho] + \sum_{\alpha} \Gamma_{\alpha} \left(L_{\alpha} \rho L_{\alpha}^{\dagger} - \frac{1}{2} \rho L_{\alpha}^{\dagger} L_{\alpha} - \frac{1}{2} L_{\alpha}^{\dagger} L_{\alpha} \rho \right) = -\frac{i}{\hbar}[H, \rho] + L(\rho). \quad (2.3)$$

In this equation, the *Lindblad operator* L_{21} , given by

$$L_{21} = |1\rangle \langle 2|, \quad (2.4)$$

weighted with the *spontaneous decay rate* Γ_{21} , includes the transition from the second to the first energy level by spontaneous decay. The way the Lindblad operators arise in this equation makes the population of the second level decrease by $-\Gamma_{21} \cdot \rho_{22}$, the population of the first level increase by $\Gamma_{21} \cdot \rho_{22}$ and the coherences decrease with a rate of $-\Gamma_{21}/2$. Decay from higher levels is treated analogously. The normalization of the density matrix is preserved with this form of the equation. For a formal introduction of the Lindblad equation see [21]. In atomic physics, the contributions of the second part of the equation are typically summarized in one matrix $L(\rho)$, which is then called Lindblad matrix or Lindblad operator.

2.1.2 Two Level System

In the simplest case, two atomic states coupled by one light field are considered. For simplicity one assumes that the light field is weak and has only one frequency

2.1 Atom Light Interaction

component. Furthermore, one supposes that the wavelength of the light is larger than the size of the atom; in this situation, the field strength can be seen as constant over the extension of the atom. Then, the density matrix ρ is given by

$$\rho = \begin{pmatrix} \rho_{11} & \rho_{12} \\ \rho_{21} & \rho_{22} \end{pmatrix}, \quad (2.5)$$

with the populations ρ_{11} and ρ_{22} of the first and the second level respectively, and the coherences ρ_{12} and ρ_{21} .

The Hamilton operator H describing the system in the rotating frame approximation is given by

$$H = \hbar \begin{pmatrix} 0 & \Omega_{12}/2 \\ \Omega_{12}/2 & -\Delta_{12} \end{pmatrix}. \quad (2.6)$$

As the frequency of the light field is scanned in the vicinity of the transition from the ground state $|1\rangle$ to an excited state $|2\rangle$, Δ_{12} is the detuning of the light field with respect to this transition frequency. Classically, the energy of a dipole in an electric field is given by the scalar product of the electric field vector with the dipole moment vector. Corresponding to that, in equation 2.6 the *Rabi frequency* Ω_{12} , given by

$$\Omega_{12} = \frac{d_{12}E_0}{\hbar}, \quad (2.7)$$

is a frequency corresponding to the energy of the electric field E_0 of the light field coupling to the *dipole matrix element* d_{12} of the atomic transition, given by

$$d_{12} = e \langle 1 | r | 2 \rangle. \quad (2.8)$$

In this equation, e is the elementary charge and r the position operator. The Rabi frequency can be rewritten using the relation

$$I = \frac{1}{2} \varepsilon_0 c E^2 \quad (2.9)$$

between intensity I and the electric field via the electric permittivity in free space ε_0 and the speed of light c . This yields

$$\Omega_{12} = \frac{d_{12}}{\hbar} \sqrt{\frac{2I}{\varepsilon_0 c}}, \quad (2.10)$$

which is more applicable than equation 2.7, as the intensity is an experimentally accessible quantity.

An important property describing the ratio of the Rabi frequency and the decay rate is the *saturation parameter*

$$S = \frac{I}{I_{\text{sat}}} = \frac{2\Omega^2}{\Gamma}. \quad (2.11)$$

2 Theoretical Background: Atomic Physics

The saturation intensity I_{sat} is given by

$$I_{\text{sat}} = \frac{\pi \hbar c}{3\lambda^3 \tau}, \quad (2.12)$$

where $\tau = 1/\Gamma$ is the lifetime of the excited state (see [22]). The probe beam on the ground state transition can be called *weak* when the saturation parameter S given in equation 2.11 is smaller than one.

The Lindblad operator $L(\rho)$ for the two level system is given by

$$L(\rho) = \Gamma_{21} \begin{pmatrix} \rho_{22} & -\frac{1}{2}\rho_{12} \\ -\frac{1}{2}\rho_{21} & -\rho_{22} \end{pmatrix}. \quad (2.13)$$

To find the steady state solution, the Hamilton operator (equation 2.6) and the Lindblad operator (equation 2.13) are inserted in the Lindblad equation (equation 2.3). The steady state solution $\dot{\rho} = 0$ leads to the steady state population of the excited state

$$\rho_{22}^{ss} = \frac{\Omega_{12}^2}{4\Delta_{12}^2 + \Gamma_{21}^2 + 2\Omega_{12}^2}, \quad (2.14)$$

the ground state

$$\rho_{11}^{ss} = 1 - \rho_{22}^{ss} \quad (2.15)$$

and

$$\rho_{21}^{ss} = \rho_{12}^{ss*} = -\frac{2\Omega_{12}(\Delta_{12} - i\Gamma_{21}/2)}{4\Delta_{12}^2 + \Gamma_{21}^2 + 2\Omega_{12}^2} \quad (2.16)$$

for the steady state coherences.

2.1.3 Absorption in a Two Level System

To observe the state of the atom, the light field interacting with it is the detected. The amount of light that is transmitted while passing through an absorbing medium of length z is given by the *Beer-Lambert law* for the electric field E

$$E(z) = E_0 e^{-\alpha z}, \quad (2.17)$$

which transforms into

$$I(z) = I_0 e^{-2\alpha z} = I_0 e^{-OD} \quad (2.18)$$

for the intensity of the light field (see equation 2.9). Here, OD is the *optical depth* of the system and α the *absorption coefficient*. For atoms at rest, the absorption coefficient is directly related to the imaginary part \Im of the *electric susceptibility* χ by

$$\alpha = k\Im(\chi). \quad (2.19)$$

For low electric field values E , the electric susceptibility χ can be treated as a constant and scales linearly with the polarization P of the medium, given by

$$P = \epsilon_0 \chi E. \quad (2.20)$$

Furthermore, the polarization of an atomic cloud is given by the sum of the polarizabilities of the single atoms p_A , which are given by the expectation value of the dipole matrix element. With the atomic density n , the polarization can be described by

$$\begin{aligned} P &= np_A \\ &= n \langle d \rangle \\ &= n(d_{12}\rho_{21} + d_{21}\rho_{12}) \\ &= 2nd_{12}\rho_{21}. \end{aligned} \quad (2.21)$$

Eliminating the polarization in equation 2.20 using equation 2.21, the susceptibility of the system yields

$$\chi = 2n \frac{d_{12}}{\varepsilon_0 E} \rho_{21}. \quad (2.22)$$

With the coherence ρ_{21} given in equation 2.16, the susceptibility and absorption coefficient finally result in

$$\chi = 2kn \frac{d_{12}}{\varepsilon_0 E} \frac{2\Omega_{12}(i\Gamma_{21}/2 - \Delta_{12})}{4\Delta_{12}^2 + \Gamma_{21}^2 + 2\Omega_{12}^2} \quad (2.23)$$

$$\alpha = 2kn \frac{d_{12}}{\varepsilon_0 E} \frac{\Omega_{12}\Gamma_{21}}{4\Delta_{12}^2 + \Gamma_{21}^2 + 2\Omega_{12}^2}. \quad (2.24)$$

Changing the detuning of the light field results in a Lorentzian absorption profile which has a width of $\sqrt{\Gamma_{21}^2 + 2\Omega_{12}^2}$. For weak beams, the decay rate Γ_{21} becomes dominant and the Lorentzian width corresponds to the *natural linewidth*. For strong light fields, large values of the Rabi frequency Ω_{12} are dominant compared to Γ_{21} . In this situation, a so-called *saturation broadening* of the line takes place.

2.1.4 Absorption in a Thermal Vapor

The setup discussed in this work deals with thermal atoms. The approximation of an atom at rest is not valid in this system and the velocity distribution needs to be taken into account. As only the component of motion projected onto the beam direction is relevant for the *Doppler effect* $\Delta_D = \vec{k}\vec{v}$, the one dimensional *Boltzmann distribution*

$$N(v)dv = N_0 \sqrt{\frac{m}{2\pi k_B T}} e^{-\frac{mv^2}{2k_B T}} dv \quad (2.25)$$

is required, with v being the value of the velocity component along the wave vector \vec{k} . The mass of the atom is m , k_B is the Boltzmann constant and T the temperature of the vapor in Kelvin. The detuning to the transition frequency is given by both the laser detuning and the detuning due to the Doppler effect. Therefore, the absorption coefficient α in a thermal vapor, with

$$\alpha = k \int \Im(\chi(\Delta - kv)) \sqrt{\frac{m}{2\pi k_B T}} e^{-\frac{mv^2}{2k_B T}} dv \quad (2.26)$$

2 Theoretical Background: Atomic Physics

is given by the convolution of the absorption coefficient of atoms at rest with the velocity distribution. This results in a *Voigt profile* which is the convolution of a Gaussian profile with a Lorentzian profile. The full width half maximum ω_D of the Gaussian component

$$\omega_D = \frac{\omega_0}{c} \sqrt{\frac{8 \ln(2) k_B T}{m}} \quad (2.27)$$

is called *Doppler width*. In this formula, ω_0 is the resonant transition frequency. The full width half maximum is $\sqrt{8 \ln(2)}$ times the standard deviation σ of the Gaussian distribution.

2.1.5 Gaussian Beam Profile

The beams in the experiments described in this work are assumed to be *Gaussian beams* with a radial intensity distribution given by [23]

$$I(r) = I_0 e^{-2r^2/w_0^2} = \frac{2P_0}{\pi w_0^2} e^{-2r^2/w_0^2}. \quad (2.28)$$

In this model, the intensity I at the radial distance r to the center depends on the total power P_0 of the beam and the beam waist w_0 . The beam waist w_0 is the $1/e^2$ diameter of the intensity distribution of the beam¹. In section 3, the intensity distribution of the light field inside hollow core fibers is discussed in more detail. With equation 2.28 and equation 2.10, the Rabi frequency

$$\Omega(r) = \frac{d}{\hbar} \sqrt{\frac{2I_0}{\varepsilon_0 c}} e^{-2r^2/w_0^2} = \frac{d}{\hbar} \sqrt{\frac{4P_0}{\pi w_0^2 \varepsilon_0 c}} e^{-2r^2/w_0^2} \quad (2.29)$$

is also depending on the radial position r . Taking this into account, the susceptibility χ as well as the absorption coefficient in equation 2.26 depend on the radial position r . Therefore, the Beer-Lambert law (equation 2.18) has to be extended to

$$I_{tot}(z) = \frac{I_0}{\pi w_0^2} \int_0^{2\pi} \int_0^\infty e^{2\alpha(r)z} e^{-2r^2/w_0^2} r \, d\varphi dr. \quad (2.30)$$

with a locally dependent absorption coefficient $\alpha(r)$.

2.1.6 Four Level System

For the Rydberg excitation in our system, the four relevant atomic levels are coupled via three light fields. The Hamilton operator H describing the system is

$$H = \hbar \begin{pmatrix} 0 & \Omega_{12}/2 & 0 & 0 \\ \Omega_{12}/2 & -\Delta_{12} & \Omega_{23}/2 & 0 \\ 0 & \Omega_{23}/2 & -\Delta_{12} - \Delta_{23} & \Omega_{34}/2 \\ 0 & 0 & \Omega_{34}/2 & -\Delta_{12} - \Delta_{23} - \Delta_{34} \end{pmatrix}. \quad (2.31)$$

¹some textbooks use the full width half maximum value

2.1 Atom Light Interaction

The variables are chosen analogously to the two level system with Ω_{ab} being the Rabi frequency of the atom light coupling of the energy levels a and b and Δ_{ab} being the detuning of the light field coupling the two levels with respect to the resonance frequency.

The energetically highest state, which will be a Rydberg state in our system, can not only decay in one of the other three atomic levels, but also into various intermediate levels not included in the model. Additionally, atoms excited to this state can crush into the fiber cladding and stick there, but desorbed atoms will most probably be in the ground state. In the reference cell, analogously, these atoms can fly out of the laser beam and be replaced by ground state atoms flying in. This will all be covered by the decay rate Γ_{41} in our model, describing the decay from the highest excited state directly into the atomic ground state.

The Lindblad operator of the four level system is given by

$$\begin{aligned}
 L(\rho) = & \Gamma_{21} \begin{pmatrix} \rho_{22} & -\frac{1}{2}\rho_{12} & 0 & 0 \\ -\frac{1}{2}\rho_{21} & -\rho_{22} & -\frac{1}{2}\rho_{23} & -\frac{1}{2}\rho_{24} \\ 0 & -\frac{1}{2}\rho_{32} & 0 & 0 \\ 0 & -\frac{1}{2}\rho_{42} & 0 & 0 \end{pmatrix} \\
 & + \Gamma_{31} \begin{pmatrix} \rho_{33} & 0 & -\frac{1}{2}\rho_{13} & 0 \\ 0 & 0 & -\frac{1}{2}\rho_{23} & 0 \\ -\frac{1}{2}\rho_{31} & -\frac{1}{2}\rho_{32} & -\rho_{33} & -\frac{1}{2}\rho_{34} \\ 0 & 0 & -\frac{1}{2}\rho_{43} & 0 \end{pmatrix} \\
 & + \Gamma_{32} \begin{pmatrix} 0 & 0 & -\frac{1}{2}\rho_{13} & 0 \\ 0 & \rho_{33} & -\frac{1}{2}\rho_{23} & 0 \\ -\frac{1}{2}\rho_{31} & -\frac{1}{2}\rho_{32} & -\rho_{33} & -\frac{1}{2}\rho_{34} \\ 0 & 0 & -\frac{1}{2}\rho_{43} & 0 \end{pmatrix} \\
 & + \Gamma_{41} \begin{pmatrix} \rho_{44} & 0 & 0 & -\frac{1}{2}\rho_{14} \\ 0 & 0 & 0 & -\frac{1}{2}\rho_{24} \\ 0 & 0 & 0 & -\frac{1}{2}\rho_{34} \\ -\frac{1}{2}\rho_{41} & -\frac{1}{2}\rho_{42} & -\frac{1}{2}\rho_{43} & -\rho_{44} \end{pmatrix}, \tag{2.32}
 \end{aligned}$$

where Γ_{ba} is the decay rate of atoms decaying from level b to level a . The decay rates Γ_{42} and Γ_{43} are set to zero, as they play a minor roll in the experiment.

A steady state solution of the Lindblad equation for the weak probe approximation is given in [24]. However, the probe beam in our experiment is not weak, so the approximation does not hold for our measurements. Hence, the steady state solution for our system needs to be found numerically.

2.2 Rydberg Atoms

For *Rydberg atoms*, the valence electron is in an excited state with a main quantum number significantly higher than for the ground state. Analogously describing a Rydberg atom quantum mechanically to a hydrogen atom is quite successful, as the distance between the core and the excited electron is large. The electron experiences an effective attraction of the core shielded by the inner electrons. One calculates the energy levels of an Rydberg atom by

$$E_n = -\frac{R}{n^{*2}} \quad (2.33)$$

with the Rydberg constant R . The *effective main quantum number* n^* , given by

$$n^* = n - \delta_p \quad (2.34)$$

covers the deviation between the hydrogen atom approximation and the Rydberg atom by subtracting the quantum defect δ_p from the main quantum number n . For the $nP_{3/2}$ states of cesium, which were addressed in this work, the quantum defect is [25]

$$\delta_p = 3.558. \quad (2.35)$$

Examples for the scaling behavior of physical properties of Rydberg atoms with respect to the effective main quantum number are shown in table 2.1.

Physical property	Scaling behavior
Orbital radius	n^{*2}
Binding energy	$1/n^{*2}$
Lifetime	n^{*3}
Dipole matrix elements	$n^{*-3/2}$
Polarizability	n^{*7}

Tab. 2.1: Scaling laws for Rydberg states depending on their effective main quantum number n^* [26].

In this work, Rydberg states with main quantum numbers between 26 and 46 have been observed. This corresponds to orbital radii in the order of 700 to 2000 times the Bohr radius a_0 , or 36 nm to 110 nm.

The scaling of the polarizability will be important to calculate the quadratic Stark effect, which describes the influence of external static electric fields on the atomic levels. For example, the polarizability of the $40P_{3/2}$ state in cesium is [27] $230.4 \text{ MHz}(\text{V}/\text{cm})^{-2}$.

2.3 DC Stark Effect

In general, the energy change δ of a dipole d when brought into a static electric field \vec{E} is

$$\delta = \vec{d}\vec{E}. \quad (2.36)$$

As wavefunctions of electrons bound in a hydrogen like atom are symmetric, they do not show a permanent dipole moment². However, the electric field induces a dipole moment

$$d_{\text{ind}} = \alpha_{\text{p}}E \quad (2.37)$$

in the atom, depending on the polarizability α_{p} . This leads to a second order contribution

$$\delta = \frac{1}{2}\alpha_{\text{p}}E^2. \quad (2.38)$$

This energy shift which is shown by atomic levels in static electric fields is called *quadratic Stark effect* or *DC Stark effect*.

²only hybrid orbitals can have a permanent dipole moment

3 Theoretical Background: Hollow Core Fibers

Common fiber optic is made of glass with two different refractive indices where the refractive index of the core is higher than the refractive index of the cladding. The light is kept inside the core by total internal reflection (TIR) on the glass-glass interface. This guiding mechanism can not work for hollow core fibers anymore, as there exists no material with a refractive index lower than the air or vacuum in the core.

3.1 Light Guidance in Capillaries

Capillaries guide the light by almost total reflection for grazing incidence. There is still some remaining transmission into the cladding layer. This leads to a sharp decline of the light transmission through the fiber when it is bent. As there is light leaking into the cladding, the energy of the light field gets partly lost. Due to this loss, there is no strict boundary condition for the light mode and one would expect a continuous spectrum of modes guided in the capillary. However, discrete modes were observed in experiments. These modes are identified with modes of non-leaky hollow waveguides. The losses into the cladding layer causes these *quasi-modes* to be non-orthogonal in contrast to the orthogonal modes in the non-leaky waveguides.

For all calculations a *cylindrical oversized waveguide* is considered which has to fulfill the conditions [28]

$$2\pi a/\lambda \gg 1 \tag{3.1}$$

$$|\lambda/\lambda_g - 1| \ll 1. \tag{3.2}$$

The waveguide is named “oversized” as first condition requests that the radius a of the capillary is significantly larger than the wavelength λ of the guided light. The second condition calls for a low damping, as the wavelength value λ_g inside the waveguide has to be close to the value λ in free space. In addition, the cladding layer is assumed to be infinitely thick.

To calculate the modal structure, one assumes a spacial field distribution at the front of the fiber and finds the quasi-modes by searching for resonance-like minimal transmission losses when the light propagates. This leads to three types of modes, which can be guided by the structure [28]:

3 Theoretical Background: Hollow Core Fibers

- *Transverse electric modes* (TE_{0p}) which show field components (for $p \leq 1$; $J_1(u_{0p}) = 0$)

$$E_\varphi \propto J_1(u_{0p}r/a) \quad (3.3)$$

$$H_r = -\sqrt{\frac{\varepsilon_0}{\mu_0}} E_\varphi \quad (3.4)$$

$$H_z = \lambda/(2\pi a) \approx 0. \quad (3.5)$$

All other electric and magnetic field components are zero for transverse electric modes.

- *Transverse magnetic modes* (TM_{0p}) which show field components (for $p \leq 1$; $J_1(u_{0p}) = 0$)

$$E_r \propto J_1(u_{0p}r/a) \quad (3.6)$$

$$E_z = \lambda/(2\pi a) \approx 0 \quad (3.7)$$

$$H_\varphi = \sqrt{\frac{\varepsilon_0}{\mu_0}} E_r. \quad (3.8)$$

All other electric and magnetic field components are zero for transverse magnetic modes.

- *Hybrid modes* (EH_{lp}) where almost all electric and magnetic field components are non-zero (for $l \neq 1; p \leq 0$; $J_{l-1}(u_{lp}) = 0$)

$$E_\varphi \propto J_{l-1}(u_{lp}r/a) \cos(l\varphi) \quad (3.9)$$

$$E_r \propto J_{l-1}(u_{lp}r/a) \sin(l\varphi) \quad (3.10)$$

$$E_z = \lambda/(2\pi a) \approx 0 \quad (3.11)$$

$$H_\varphi = \sqrt{\frac{\varepsilon_0}{\mu_0}} E_r \quad (3.12)$$

$$H_r = -\sqrt{\frac{\varepsilon_0}{\mu_0}} E_\varphi \quad (3.13)$$

$$H_z = 0 \quad (3.14)$$

In this equations, μ_0 is the vacuum permeability. The electric field components E and the magnetic field components H receive the indices r for the radial, φ for the azimuthal and z for the axial components. The u_{lp} are the p^{th} root of the J_{l-1} Bessel function of the first kind. The l -value is the number of periods of the magnetic and electric field components in the azimuthal direction - which means the number of lines to which the field is mirror-symmetric. In [29], a more precise form of the field components is given.

In figure 1, electric field lines for a set of modes in hollow core fibers are shown. For the TE_{01} and TE_{02} modes, the graph of the J_1 Bessel function - plotted below

3.1 Light Guidance in Capillaries

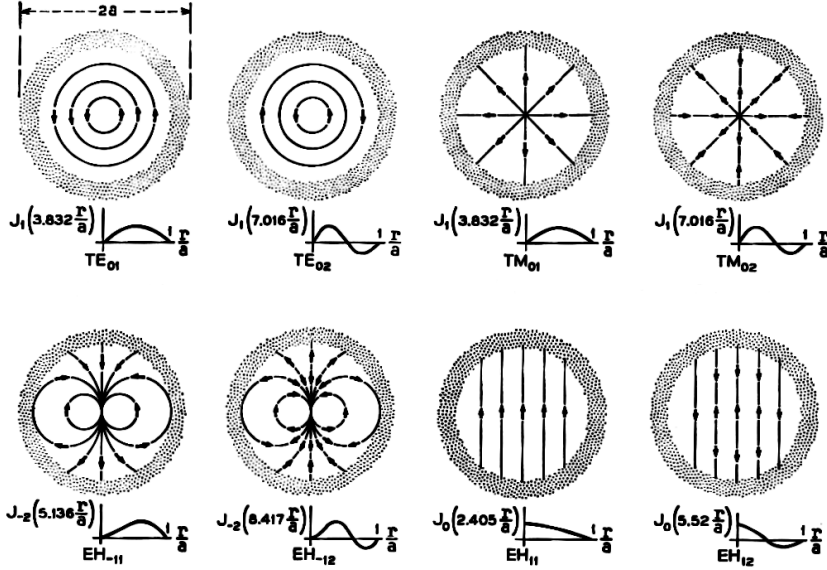


Fig. 1: Modal structure of the light field in hollow core waveguides for transverse electric modes (TE), transverse magnetic modes (TM) and hybrid modes (EH) [29].

the mode picture - are proportional to the strength of the azimuthal field component. In the case of the TM_{01} and TM_{02} modes it is proportional to the amplitude of the radial field component. The hybrid mode EH_{11} is the most important in our case as Gaussian beams can only excite EH_{1m} modes [30]¹ and the EH_{11} mode is the one having the lowest theoretical loss. The field distribution of this mode is also the most comparable to the field distribution of a free Gaussian beam.

In order to find the power coupling efficiency to the EH_{11} mode, the overlap integral between the electric field mode

$$E(r) = E_0 J_0(u_{11} r/a) \quad (3.15)$$

and electric field of the Gaussian Beam

$$E(r) = E_0 e^{-r^2/w_0^2} \quad (3.16)$$

is calculated as it is demonstrated in [30]. The overlap integral is then given by

$$\eta_{11} = \frac{\left[\int_0^a e^{-r^2/w_0^2} J_0(u_{11} r/a) r dr \right]^2}{\int_0^\infty e^{-2r^2/w_0^2} r dr \int_0^a J_0^2(u_{11} r/a) r dr} \quad (3.17)$$

¹Note that both [28] and [29] use a convention where all hybrid modes are labeled EH_{lp} and l can be both positive or negative. The more common way in current research, which is also used in [30] is, to label the modes with positive l -values as HE_{lp} modes and the ones with negative l -values as EH_{lp} modes without writing the minus.

3 Theoretical Background: Hollow Core Fibers

and results for the best overlap

$$w_0/a \approx 0.64 \longrightarrow \eta_{11} = 0.981. \quad (3.18)$$

Therefore in the experiment, the beams were focused on the fiber end, trying to achieve a focus beam waist of $0.64a$ to reach high coupling efficiencies.

3.2 Kagomé Hollow Core Photonic Crystal Fibers

In photonic crystal fibers, a periodic pattern of holes in the glass wall around the core region leads to a modal structure with photonic bandgaps [11]. This is similar to electronic bandgaps in solid state physics occurring in periodically ordered materials due to Bragg reflection. Light can not escape from the core region of a photonic crystal fiber when its wavelength is in the bandgap of the surrounding structure. A schematic cross section of such a hollow core photonic bandgap fiber (HC-PBG) is shown in figure 2a.

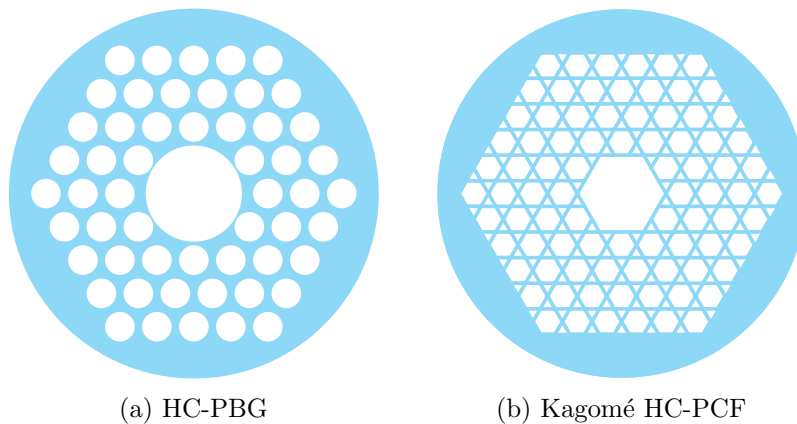


Fig. 2: Schematic cross section of hollow photonic crystal fibers.

When the periodic photonic crystal pattern is changed to a kagomé lattice, no sharp bandgaps can be seen anymore and a rather broadband light guidance is obtained. In figure 2b the structure of such a kagomé hollow core photonic crystal fiber (kagomé HC-PCF) is shown schematically. The thickness of the glass around the core is only a few hundreds of nanometers, whereas it is in the order of micrometers or more for capillaries. Another significant difference to capillaries is the not circular but hexagonal core. In contrast to capillaries, light guidance in hollow core photonic crystal fibers remains the same when the fiber is bent. A scanning electron microscope picture of such a kagomé hollow core photonic crystal fiber is shown in figure 3.

To get the exact solution for the light guidance inside a kagomé hollow core photonic crystal fiber, numerical models [31] are needed. However, in [32] it is shown

3.2 Kagomé Hollow Core Photonic Crystal Fibers

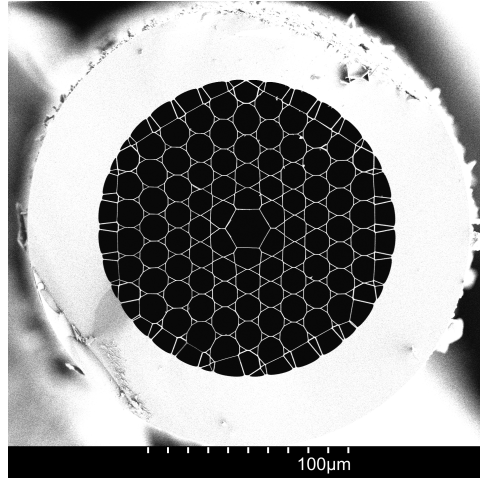


Fig. 3: Example of a kagomé hollow core photonic crystal fiber: SEM picture of the cross section (picture provided by the MPL Erlangen). White regions are glass walls, whereas the holes of the fiber are black. The core in the center of the fiber is surrounded by the photonic crystal glass structure. This is protected by the glass cladding around it.

that the model for the light guidance in capillaries can be applied to some extent for the kagomé hollow core photonic crystal fibers as well. For the capillary radius associated with the core size of the kagomé fiber the *area-preserving radius* r_{AP} is used. This is the radius of a circle having the same area as the hexagon of the kagomé fiber core and is calculated by

$$r_{\text{AP}} = r_{\text{FF}} \sqrt{\frac{2\sqrt{3}}{\pi}} \approx 1.05 r_{\text{FF}}, \quad (3.19)$$

where r_{FF} is the *flat-to-flat radius* between to opposing core walls. The main deviations to the capillary modes arise from the small wall thickness t . To face this problem, an effective core radius is introduced empirically in [32] which leads to a critical wavelength λ_{crit} given by

$$\lambda_{\text{crit}} = 0.98 \sqrt{2r_{\text{AP}}t}. \quad (3.20)$$

For wavelengths longer than that, the deviations between the group velocity delay due to the modal structure of the field in the kagomé HC-PCF and the capillary exceed 15%. This deviations are caused by the light field being partly guided in the glass and the holes outside the core, which is increased for long wavelengths. For the fibers and wavelengths we use in our experiment, this 15% deviation are never exceeded, and the simple capillary model can be applied.

3.3 Light Induced Atomic Desorption

For every system with an atomic vapor trapped between walls, there is a ratio between atoms desorbed from and adsorbed to the confining surfaces. This leads to a specific vapor pressure in the system which depends on its temperature only. When light is shone on the surface, an additional effect, the light induced atomic desorption (LIAD) takes place. This effect was first reported in [33] in macroscopic vapor cells. In a hollow core fiber, the regions of high light intensity are intrinsically very close to the surface. Together with a much larger surface to volume ratio than for macroscopic vapor cells, one can expect the effect to be more pronounced. It was shown in [14] that LIAD can lead to a significant change in the vapor pressure inside a hollow core fiber.

When a cesium atom reaches the surface, there are four different cases that can occur. The first is, that the atom directly sticks to the glass wall. Secondly, the atom can stick on other cesium atoms which are already adsorbed and form clusters. Also, it can diffuse into the glass material or finally can just bounce off.

This leads to several possible processes with different time scales and energy scales that can take place when the surface is illuminated with light of a specific wavelength and intensity. The first possible process is the desorption of the atom from the wall, where the photon provides the energy to overcome the binding energy between the cesium atom and the surface. The result of this process is a non-equilibrium condition of cesium bound deeper in the glass afterwards. Therefore, cesium atoms sitting deep inside the glass propagate closer to the surface and can be desorbed as well. The binding energy of the atoms on the glass surface can vary for different positions on the surface, depending on the environment. The higher the energy of the single photons the higher the probability to desorb a single atom from the wall. Hence, this process is enhanced when the desorption is induced by light of shorter wavelength. This direct desorption - similar to the photo effect - is what typically is referred to as LIAD. However, LIAD is sometimes also used as a generic term for all kind of processes of desorbing atoms from a surface via light.

A second process taking place when light is shone on a surface is heating of cesium clusters on top of the glass by exciting plasmonic resonances. This process was named surface-plasmon-induced desorption (SPID) by Moi and coworkers [34]. How many atoms get desorbed by this process depends on how well the resonance frequency is hit by the light. The difference between desorption by LIAD and SPID is discussed and experimentally investigated in [34].

4 Experimental Setup

The experimental details of this work are presented in this chapter. The relevant physical properties of cesium are introduced in the first part of this chapter. Then the excitation scheme applied, as well as the laser setups for the three lasers involved are shown in section 4.2. In the third part of this chapter, the setup of the three photon spectroscopy is shown and technical details are explained. Finally, characteristics of the fibers used for the experiments are presented in section 4.4.

4.1 Cesium

All results reported in this thesis were performed in a thermal cesium vapor. The numbers and formulas given in this chapter are cited from [35]. One advantage of using the alkali metal cesium is that only one stable isotope ^{133}Cs exists. It has a nuclear spin of

$$I = 7/2, \quad (4.1)$$

which leads to a hyperfine splitting of 9.193 GHz for the $6S_{1/2}$ state and 1.168 GHz for the $6P_{1/2}$ state. This splitting is larger than the Doppler width (equation 2.26) at room temperature, which is about 360 MHz. Therefore, the laser locked on the D1 line only excites electrons from one ground state hyperfine level to only one hyperfine level of the excited state. For example for rubidium this locking scheme is not possible at room temperature.

The melting point of cesium is

$$T_m = 28.5^\circ\text{C}, \quad (4.2)$$

which leads to a relatively large vapor pressure at room temperature. Typical temperatures used in our experiments were 60°C for the reference cell and room temperature for the fibers. To find the vapor pressure at these temperatures, the numerical formula

$$P_v = 10^{4.165-3830/T} \quad (4.3)$$

is used, where T is the temperature in Kelvin and P_v is the vapor pressure in atmospheres. This formula results in 4.6×10^{-8} atm (1.7×10^{-9} atm) for the experiment at 60°C (room temperature), respectively. Using the ideal gas law $PV = Nk_B T$ one gets¹

$$n = \frac{N}{V} = \frac{P_v}{k_B T} = \frac{1}{k_B T} 1.0133 \times 10^{9.165-3830/T} \quad (4.4)$$

¹with the pressure in pascal = 1.0133×10^5 atm and the temperature in Kelvin

4 Experimental Setup

for the atomic density n in atoms per cubic meter. At room temperature, this results in $4 \times 10^{16} \text{ m}^{-3}$ (or $4 \times 10^{12} \text{ cm}^{-3}$). For 60°C the vapor pressure is $1 \times 10^{18} \text{ m}^{-3}$ (or $1 \times 10^{14} \text{ cm}^{-3}$).

4.2 Excitation Scheme and Laser Setup

The excitation scheme used in the experiment is shown in figure 4. The electron was excited from the cesium ground state to $n\text{P}_{3/2}$ Rydberg states with a three photon excitation. This excitation scheme was chosen because the fibers used in the experiment show good guiding properties for infrared wavelengths.

With the probe laser, the electron was excited from the $6\text{S}_{1/2}$ ground state to the excited state $6\text{P}_{1/2}$ (D1 line), corresponding to the Rabi frequency Ω_{12} . The probe

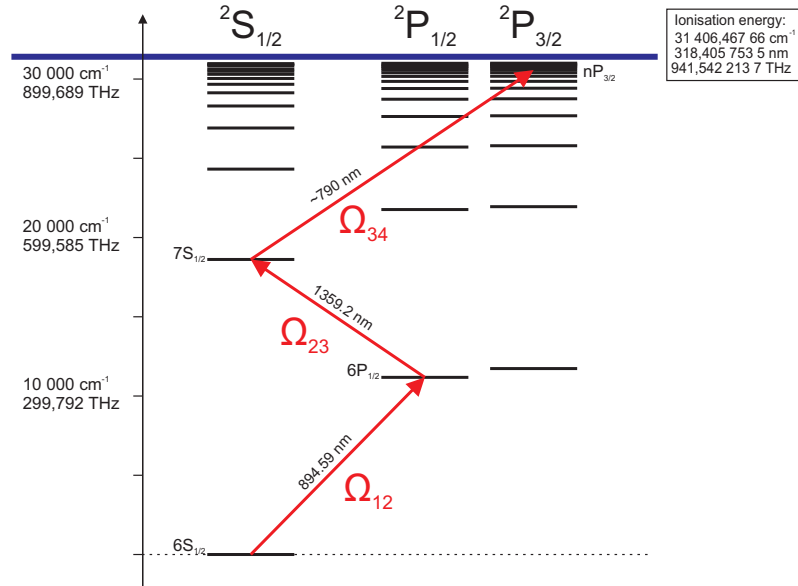


Fig. 4: Three photon excitation scheme in cesium. The electron is excited from the $6\text{S}_{1/2}$ ground state to the $6\text{P}_{1/2}$ by the probe laser with a wavelength of about 895 nm. The intermediate laser with a wavelength of 1359 nm couples this level to the $7\text{S}_{1/2}$ state from where the Rydberg coupling laser with a wavelength of 790 nm excites the electron to the $n\text{P}_{3/2}$ Rydberg state.

laser with a wavelength of 894.59 nm was a Toptica DL 100 pro design, which is a grating stabilized diode laser and has a maximum output power of 34 mW.

For the three photon excitation, the probe laser was frequency stabilized to sub-doppler accuracy on the transition the $6\text{S}_{1/2}$, $F = 3$ to $6\text{P}_{1/2}$, $F = 4$ transition. This was done by saturated absorption spectroscopy, the setup of which is shown in figure 5. If needed, the two acousto-optic modulators (AOM) included in the setup could

4.2 Excitation Scheme and Laser Setup

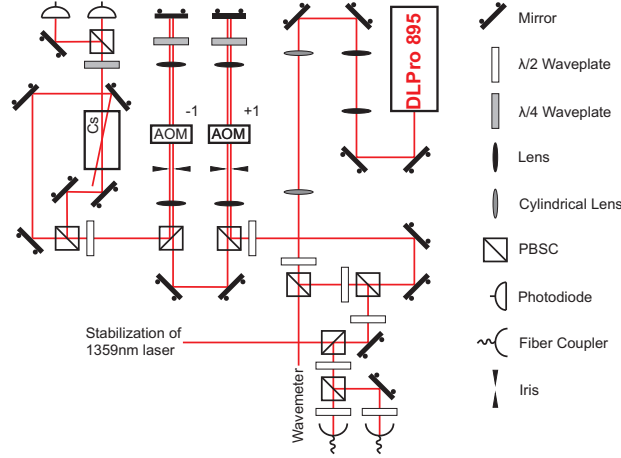


Fig. 5: Sketch of the setup to frequency stabilize the 895 nm laser system.

provide an off-resonant locking scheme. As this was not needed for the purpose of this work, they were aligned in a way that the frequency shift caused cancels out.

The light for the intermediate transition corresponding to the Rabi frequency Ω_{23} in the excitation scheme was provided by a grating stabilized diode laser Toptica DL 100 pro design and has a wavelength of 1359.2 nm. The maximum output power of this laser is 53.2 mW. In figure 6 the laser setup is shown. The laser was frequency

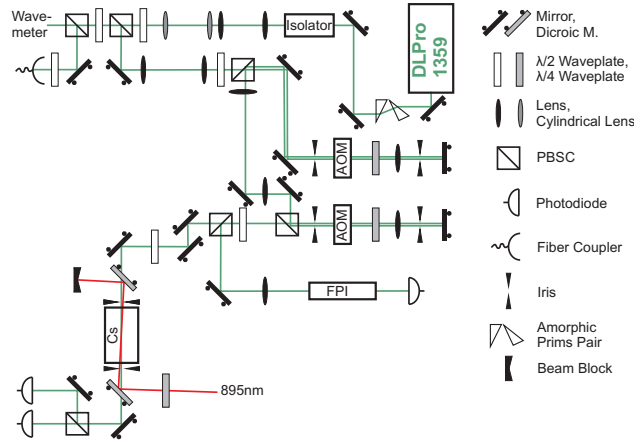


Fig. 6: Sketch of the setup to frequency stabilize the 1359 nm laser system.

stabilized to the transition from the $6P_{1/2}$, $F = 4$ to the $7S_{1/2}$, $F = 4$ state using polarization spectroscopy on the excited state transition the way it is discussed in [36]. Again, the acousto-optic modulators were operated to cancel out the frequency shift, except for the very last measurement presented in section 7.4. To ensure that

4 Experimental Setup

the laser was running single mode, a silver mirror Fabry-Perot interferometer was built in.

For the transition to the Rydberg state a Toptica DL pro with a center wavelength of 780.24 nm and a maximum output power of 84.0 mW was scanned in the vicinity of a Rydberg line. The light was amplified by a Eagleyard tapered amplifier diode² with up to 1 W output power. To scale the frequency scanning of the laser its light was sent through a Fabry-Perot interferometer with a free spectral range of 514 MHz. This interferometer was length stabilized to a frequency locked laser at 780 nm used for a different experiment to make the length of the interferometer temperature independent. Therefore, the peak position with respect to the laser trigger output only changed, when the laser frequency changed, but not when temperature variations would have changed the length of the Fabry-Perot interferometer. Hence, the oscilloscope was triggered to one of the Fabry-Perot peaks to make sure that the trigger position was always at the same frequency, even when the frequency scan of the laser moved due to temperature variations during the averaging process. All the components are shown in the setup picture in figure 7. There were two optical

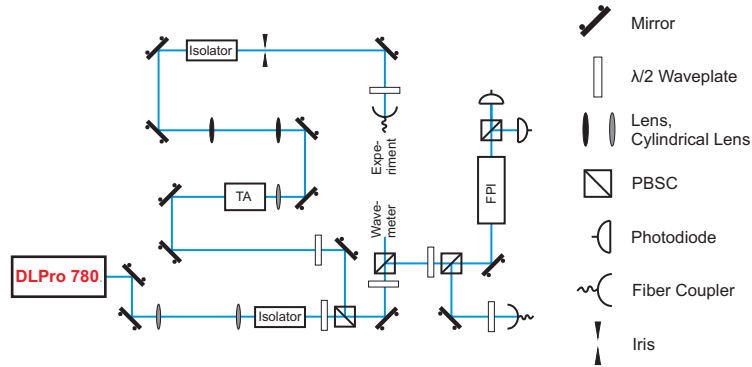


Fig. 7: Sketch of the setup of the amplified 780 nm laser system and the frequency reference by a Fabry-Perot interferometer.

isolators built in, in addition to the one inside the laser. One prevents the laser against back reflections and fluorescence from the tapered amplifier. The other prevents the tapered amplifier against back reflections from the fiber coupler. As the Rydberg coupling laser was a diode laser at an infrared wavelength, changing the main quantum number of the Rydberg excitation was technically less challenging than for the typically used two photon setup, were the wavelength of a frequency doubled blue laser needs to be changed.

Values corresponding to the probe laser at 895 nm will be marked by an index P and those for the intermediate laser at 1359 nm and the Rydberg coupling laser at around 790 nm by an I and C respectively.

²Model: EYP-TPA-0780-01000-3006-CMT03-000

4.3 Setup of the Three Photon Spectroscopy

All three laser beams were brought to the optical table where the experiment was performed via glass fibers. In figure 8, the experimental setup is shown for both, the spectroscopy in the reference cell and the fiber. The beams were overlapped using dichroic mirrors. While the probe beam was sent in one direction, split off and recorded on a photodiode, both the intermediate and the coupling laser were aligned counter-propagating to partly cancel for the Doppler effect. The polarization of all three beams was prepared linear and horizontal using polarizing beam splitter cubes.

For the reference spectroscopy, the focused beams were aligned through a pinhole with a radius of $50\ \mu\text{m}$, then the pinhole was taken out and the $5\ \text{mm}$ commercial cesium filled cell was built in. The reservoir of the cell was heated to $60\ ^\circ\text{C}$ using resistance wire. The cell itself was kept at about $80\ ^\circ\text{C}$ to prevent cesium condensation on the glass. In order to get a good signal, the three beams were focused into the reference cell by lenses with a focal length value of $f = 100\ \text{mm}$. This led to $1/e^2$ beam radii of $w_P = 41.1(10)\ \mu\text{m}$, $w_I = 64.3(12)\ \mu\text{m}$ and $w_C = 46.3(16)\ \mu\text{m}$.

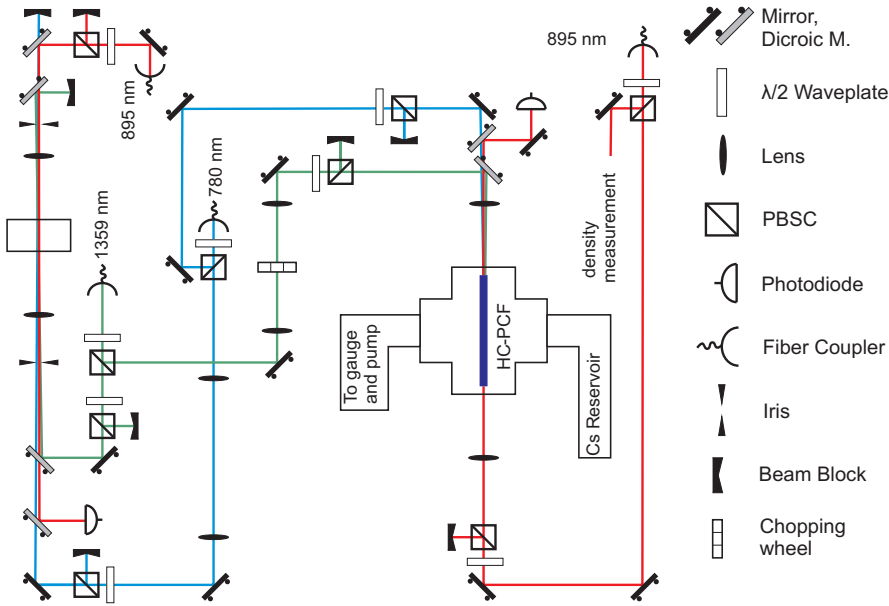


Fig. 8: Sketch of the experimental setup to perform three photon Rydberg spectroscopy in the fibers and the reference cell.

For measurements inside the fiber, the vacuum setup described in [37] was used to expose the fibers to a cesium atmosphere. The laser beams were coupled into a fiber by focussing the beams on the fiber ends using achromatic lenses. To make sure the light was coupled into the fundamental mode of the fiber, the end of the fiber was imaged by a ccd camera and the coupling efficiency was measured. For

4 Experimental Setup

this setup, the directions and the polarization of the beams was the same as in the reference setup.

To get a better signal to noise ratio, the signal of the probe beam detected on the photodiode was fed through a lock-in amplifier. Therefore in the first measurement series, the intermediate beam was modulated with a frequency of 1.1 kHz using a chopping wheel. At this point, it was not clear on which timescale the optical depth changes when the coupling light is switched on and off again. But, no influence of the intermediate laser on the optical depth was seen.

After the light induced atomic desorption (LIAD) measurements reported in section 6 were performed, the setup was changed. These measurements showed that modulating the coupling beam with a frequency of 50 kHz with an AOM would not cause a modulation in the optical depth. One advantage of this modulation scheme is, that modulation the coupling beam only affects the signal but not the background. Additionally, the laser could be scanned faster in frequency as the modulation frequency is higher. Therefore, more spectra could be taken and averaged in the same time and the quality of the signal could be improved.

4.4 Fibers used in the Experiment

4.4.1 HC-PCF with 60 μm and 19 μm core size

Most measurements shown in this work were performed in two kagomé hollow core photonic crystal fibers. A 3 row kagomé HC-PCF with a core diameter of about 60 μm and a 5 row kagomé HC-PCF with a core diameter of 19 μm were used. Both

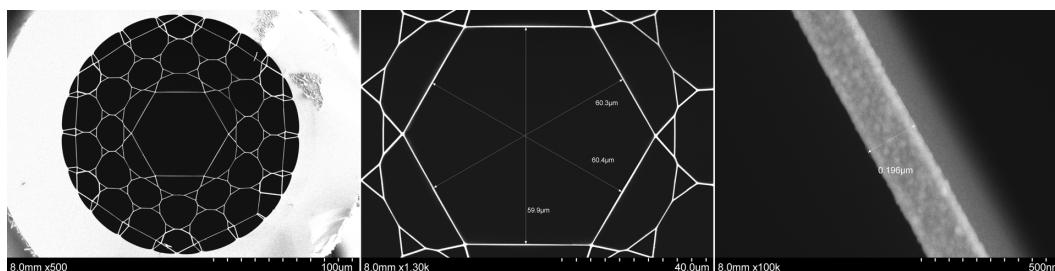
Property	60 μm core size	19 μm core size
Distance between core walls	59.9 μm to 60.4 μm	19.1 μm to 19.3 μm
Flat-to-flat radius	$r_{\text{FF}} = 30.1 \mu\text{m}$	$r_{\text{FF}} = 9.6 \mu\text{m}$
Area-preserving radius of core	$r_{\text{AP}} = 31.6 \mu\text{m}$	$r_{\text{AP}} = 10.1 \mu\text{m}$
Beam waist of fundamental mode	$w_0 \approx 20.2 \mu\text{m}$	$w_0 \approx 6.5 \mu\text{m}$
Wall thickness	193 nm to 196 nm	214 nm to 228 nm
Height of triangle	$h = 5.2 \mu\text{m}$	$h = 3.8 \mu\text{m}$
Area-preserving radius of triangle	$r_t = 2.23 \mu\text{m}$	$r_t = 1.65 \mu\text{m}$

Tab. 4.1: Properties of the two kagomé hollow core photonic crystal fibers used in the experiment.

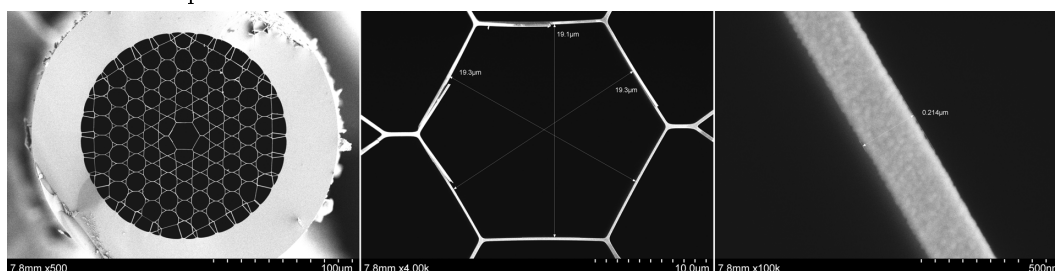
fibers were manufactured by the Max Planck Institute for the Science of Light in Erlangen (Germany).

Pictures of the cross section taken by a scanning electron microscope are shown in figure 9a for the 60 μm fiber and in 9b for the 19 μm fiber, respectively. The properties of the fibers are given in table 4.1.

4.4 Fibers used in the Experiment



(a) A 3 row kagomé structured hollow core photonic crystal fiber with an inner core diameter of about $60 \mu\text{m}$.



(b) A 5 row kagomé structured hollow core photonic crystal fibers with an inner core diameter of $19 \mu\text{m}$.

Fig. 9: Scanning electron micrographs of fronts of the fibers used. The left picture shows the complete cross section of the fiber. In the middle, only the core region is displayed and the core diameter for different opposing walls is inserted. Further zooming in resolves the walls, which are shown in the left picture.

The plastic coatings of the fibers were removed and the fibers were cleaved to a length of 135 mm. All fibers were fixed on a self-built fiber holder in the ultra high vacuum chamber and exposed to a cesium atmosphere. The light was coupled into the fiber with a core size of $60 \mu\text{m}$ using achromatic lenses with a focal length value of $f = 100 \text{ mm}$. A transmission in the fundamental mode of $\approx 40 \%$ (895 nm), $\approx 30 \%$ (1359 nm) and $\approx 60 \%$ (790 nm) of the incoming light power could be achieved. For the kagomé HC-PCF with a core diameter of $19 \mu\text{m}$ incoupling lenses with a focal length value of 40 mm were used. The transmission of the incoming light power was in the order of $\approx 30 \%$ (895 nm), $\approx 20 \%$ (1359 nm) and $\approx 40 \%$ (790 nm).

In figure 10, three levels of the coupling process can be seen. By optimizing the position and angle of the incoupling beam and lens, the light can be coupled into the fundamental mode of the fiber. Images of the outcoming light were recorded by a camera behind the fiber. In the left picture of figure 10, the light is mostly coupled into the glass cladding of the fiber as the position and angle of both the beam and the incoupling lens is not optimized. Improving the parameters, light guidance in the photonic structure can be observed which is shown in the middle picture. One can see that the light is partly coming out of the cladding layer but is also guided through the small holes of the photonic crystal structure between the core and the

4 Experimental Setup

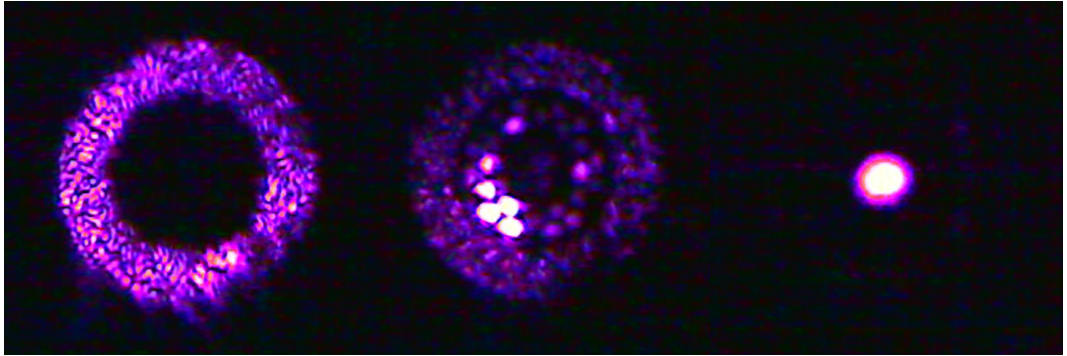


Fig. 10: Three different levels of the coupling process are shown. In the left picture, all light reaching the camera is guided in the glass cladding surrounding the photonic crystal structure. Turning the beam closer to the center of the fiber, light guidance in holes of the photonic structure neighboring the fiber core can be observed, as shown in the middle picture. After the optimization of the beam position and angle as well as the position of the incoupling lense the beam propagates in the core of the fiber, as shown in the right picture.

cladding. When the beam and the lens are optimized, the light is all guided in the core of the fiber as shown in the right image of figure 10. The mode is assumed to be the fundamental mode EH_{11} of the fiber. As this mode has the highest transmission coefficient, the incoupling is not only optimized by observing the outcoming beam profile, but also by maximizing the output power.

4.4.2 Capillary with 70 μm core size

In addition to the kagomé HC-PCF, a capillary has been used as well. It was a capillary with an inner core diameter of 70 μm . The fiber was cleaved by first making a little scratch on the surface with a razor blade and then breaking it. As the HC-PCF, it has a length of 135 mm, is mounted on a fiber holder, put into the vacuum chamber and exposed to the cesium atmosphere. The capillary was produced by the Institut für Strahlwerkzeuge at the Universität Stuttgart. Similar capillaries were investigated in [38], where pictures of the cross section are shown and the coupling process is described in more detail.

For the capillary with a core diameter of 70 μm , the corresponding beam waist of the fundamental mode is $w_0 \approx 22.4 \mu\text{m}$. Therefore, incoupling lenses with a focal length value of 100 mm were used. The transmission of the incoming light power was in the order of $\approx 8\%$ (1359 nm) and $\approx 40\%$ (790 nm). The transmission of the laser at 895 nm was not measured, but is estimated to be in the order of 10% – 20%.

4.5 Optical Depth in Hollow Core Fibers

The optical depth of the system, defined in equation 2.18, describes the absorption of light by the medium. In this work, the given optical depth values correspond to the optical depth of the cesium vapor when the the laser light is on resonance with the $6S_{1/2}, F = 3$ to $6P_{1/2}, F = 4$ transition. This transition was chosen, as the probe laser is frequency stabilized on it, when the Rydberg spectroscopy is performed. The optical depth was measured by scanning the probe laser in the vicinity of the D1 line and fitting the received transmission signal. As the Doppler broadening is the dominant broadening mechanism in a thermal vapor, a purely Gaussian line shape was fitted to the spectrum.

To find the optical depth inside the fiber, first data is analyzed when the light is coupled into the glass cladding. The optical depth value corresponds to the absorption that takes place between the window of the vacuum chamber and the fiber ends and will be from now on named OD_{cladd} . Afterwards, the total optical depth OD_{tot} is measured for the light coupled into the core of the fiber. The absorption inside the fiber as well as the absorption between the window of the vacuum chamber and the fiber ends contribute to this value. The optical depth for coupling the laser light into the cladding is typically more than one order of magnitude smaller than the value achieved inside the core. Therefore, one can assume that the signal was dominated by atoms inside the fiber. For the measurements, the final optical depth value OD inside the fiber only, is given by the difference of the two measured numbers. Due to uncertainties in the measurement, the values for the optical depth were rounded.

One source for these uncertainties is that the optical depth is only a constant for intensities below the saturation intensity (see equation 2.12), which is $I_{\text{sat}} = 33.4 \text{ W/m}^2$ for the $6S_{1/2}, F = 3$ to $6P_{1/2}, F = 4$ transition. Using the beam areas corresponding to the $1/e^2$ radii of the beams, the beam power should be less than $P_{\text{sat},60 \mu\text{m}} = 39 \text{ nW}$ and $P_{\text{sat},19 \mu\text{m}} = 4 \text{ nW}$ for the kagomé HC-PCF and $P_{\text{sat},70 \mu\text{m}} = 53 \text{ nW}$ for the capillary. The powers used were mostly not below this value, as the noise of the background light dominated over the beam light incident at the photodiode. In addition, some optical components of the setup show a strong frequency dependent behavior when the light power is reduced so far. Therefore, the background of the absorption spectrum showed non-linear contributions, leading to additional uncertainties when fitting the spectra.

5 Diffusion of Cesium Vapor into Fibers

The initially evacuated hollow core fibers are exposed to a cesium atmosphere while lying inside the vacuum chamber. From this moment on, the atoms start to diffuse into the fiber. The process can not be described by a simple thermal motion of the atoms, but adsorption and desorption processes from the fiber walls need to be taken into account as well. After long exposure times, an equilibrium between atoms adsorbed and desorbed from the fiber walls and the background pressure of the chamber can be reached.

There are different regimes for diffusion processes (see [39]). Which mathematical model can be applied depends on the ratio of the mean free path of a particle in the gas until it collides with another atom and the relevant physical length scale of the system. This ratio, the *Knudsen number* Kn , is given by

$$Kn = l_m/r. \quad (5.1)$$

In this equation the mean free path is denoted by l_m and the relevant physical length scale which is the radius r of the capillary in our case. Using the vapor pressure P_v , according to equation 4.3, the mean free path at room temperature, is given by

$$l_m = \frac{k_B T}{\sqrt{2}\pi d^2 P_v}. \quad (5.2)$$

With the atomic diameter $d = 5.96 \text{ \AA}$ [40] of cesium the mean free path l_m is about 10 m, which is much larger than the capillary radius r . This leads to a Knudsen number significantly larger than one, which corresponds to the free molecular flow regime, where collisions between atoms can be neglected, while collisions with the fiber walls dominate. The diffusion into capillaries in the free molecular flow regime was discussed by Clausing in [41]. As presented there, the process can be described by the one dimensional diffusion equation

$$\frac{dn}{dt} = D \frac{d^2 n}{dx^2}, \quad (5.3)$$

where n is the atomic density. The diffusion constant D is given by [41]¹

$$D = \frac{4r^2}{6r/u + 3\tau}, \quad (5.4)$$

¹In [42] a formula is given which even includes surface migration of the atoms. However, it is not clear what the mean free path on the surface is in the case of cesium on quartz

5 Diffusion of Cesium Vapor into Fibers

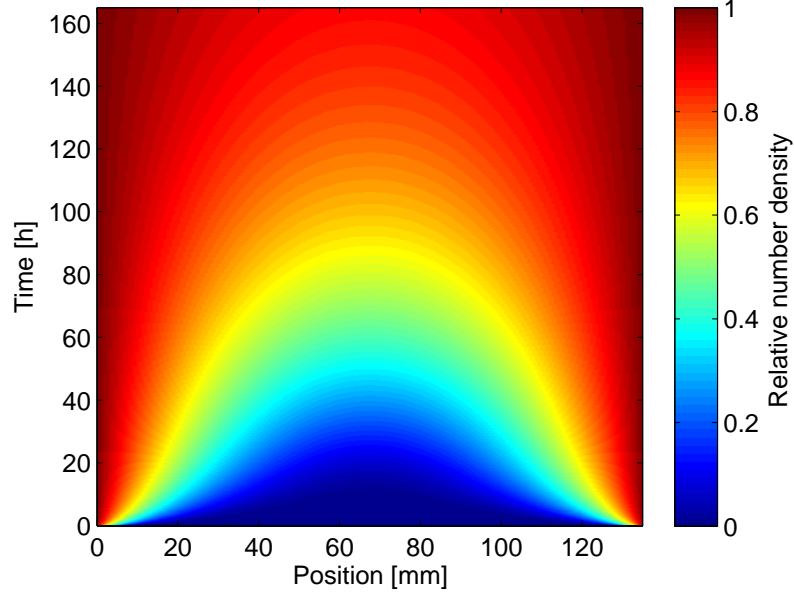


Fig. 11: Solution of the diffusion equation including adsorption of cesium on quartz. For a capillary with 19 μm diameter, 135 mm length, open on both ends, at room temperature.

where τ is the *time of adsorption* and u is the *mean velocity*

$$u = \sqrt{\frac{8k_{\text{B}}T}{\pi m}} \quad (5.5)$$

of the atoms. The mean velocity u at room temperature is in the order of 220 m s^{-1} . The time of adsorption depends on the temperature T_{W} of the fiber walls and the adsorption energy E_{a} and is given by [43]

$$\tau = \tau_0 e^{\frac{E_{\text{a}}}{k_{\text{B}}T_{\text{W}}}}. \quad (5.6)$$

For the adsorption energy value of cesium on quartz, [43] gives $E_{\text{a}} = 0.66(5) \text{ eV}$ and τ_0 is in the order of $1 \times 10^{-13} \text{ s}$. This leads to a time of adsorption in the order of $\tau \approx 15 \text{ ms}$ at room temperature and the diffusion constant results in $D = 3 \times 10^{-8} \text{ m}^2/\text{s}$ for a capillary with a radius of $r = 20 \mu\text{m}$. In figure 11, the relative number density in comparison to the background pressure is shown depending on the exposure time, for each longitudinal position in the fiber. The diffusion was calculated at room temperature for a capillary with a radius of $9.5 \mu\text{m}$ and a length of 135 mm, corresponding to the core of the kagomé HC-PCF with 19 μm core diameter, used in the experiment. While the atomic density raises quickly at the edge, the center of the fiber can still be seen as empty, even after several hours.

As all atoms along the fiber contribute to the spectroscopic signal, the mean relative number density inside the fiber is shown in figure 12 for the same parameters as in figure 11. In the right plot of figure 12 the mean filling of the fiber is shown

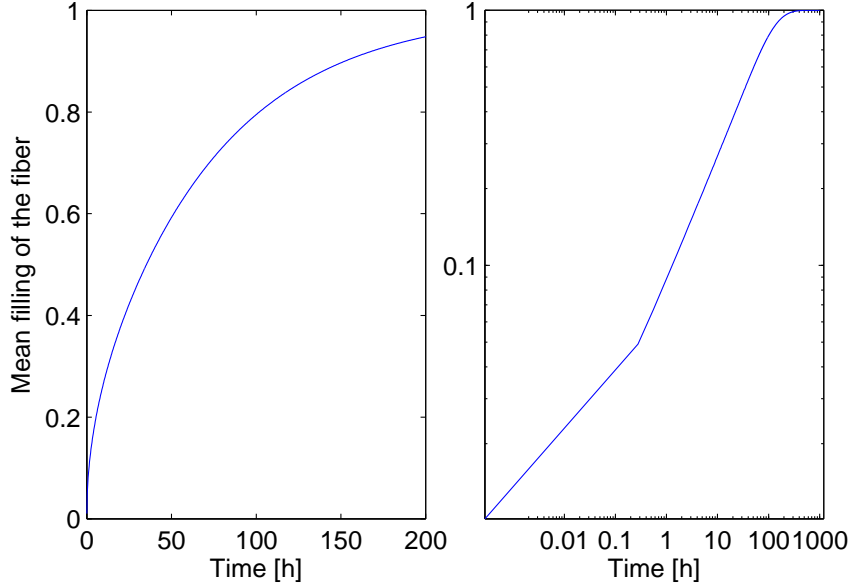


Fig. 12: Solution of the diffusion equation including adsorption of cesium on quartz. For a capillary with 19 μm diameter, 135 mm length at room temperature. The mean relative number density inside the fiber is shown in a linear (left) and a logarithmic (right) plot.

on a logarithmic scale. It seems that the diffusion process needs to be discussed in two different regimes, where different scaling laws can be seen separated by a clear kink. How the timescales are related to the parameters of the diffusion equation needs further investigation.

In this thesis, a fiber is called “completely filled” when the number density at every position is more than 85 % of the background number density in the vacuum chamber. The time needed to fill the fiber is

$$t_{85\%}(r, l, T) = 0.216 \frac{l^2}{D} \quad (5.7)$$

$$= 0.162 \left(\frac{2l^2}{ru} + \frac{l^2\tau}{r^2} \right). \quad (5.8)$$

For the fiber with 60 μm core size and 135 mm length, this results in approximately 14 h to fill the core and 120 d to fill the triangular holes for room temperature. For the fiber with 19 μm core size and 135 mm length at room temperature, approximately 6 d to fill the core and 220 d to fill the triangular holes is needed.

6 Measurements on Light Induced Atomic Desorption

To measure how the vapor pressure changes due to LIAD or SPID typically a weak probe beam is used together with a strong second beam which evokes the desorption. The probe beam is either scanning in the vicinity of an atomic transition or frequency stabilized on a transition to measure the change in the atomic density via the change in the on-resonance absorption.

In our setup, the role of the weak probe beam is taken by a laser tuned on the transition from the $6S_{1/2}$ to the $6P_{1/2}$ state. A second laser with a wavelength of about 780 nm was used to evoke the desorption as it is the laser with the most output power available. It will be referred to as “LIAD beam” from now on. All the measurements were performed in the kagomé hollow core photonic crystal fiber with a core diameter of 19 μm , as it has the greatest surface to volume ratio of the fibers in use.

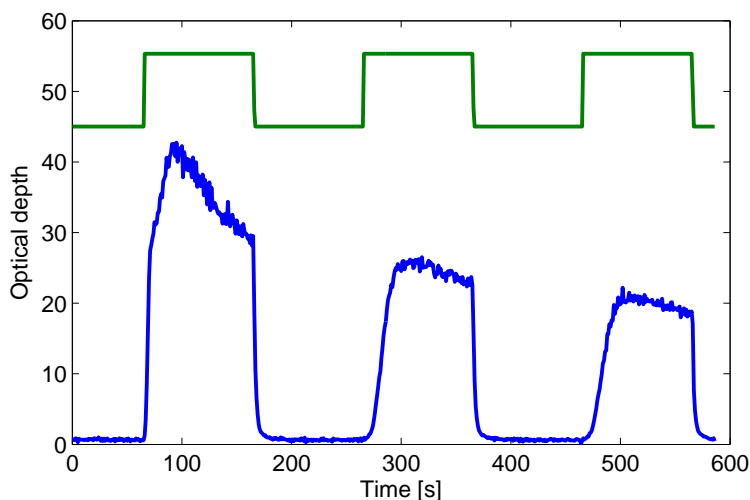


Fig. 13: Change in the optical depth in the HC-PCF with 19 μm core size for desorption pulses of 100 s. The green line shows when the LIAD beam is switched on and off. The change of the optical depth in the fiber is shown by the blue line. The beam powers were set to $P_P = 0.5 \mu\text{W}$ and $P_{\text{LIAD}} = 20 \text{ mW}$.

The data shown in figure 13 was taken to see whether at all and to what extend

6 Measurements on Light Induced Atomic Desorption

an increase of the optical depth in the fiber occurs, caused by the LIAD beam. The probe beam was set to $0.5 \mu\text{W}$ which corresponds to $0.09 \mu\text{W}$ behind the fiber. The LIAD beam was set to 20 mW resulting in 4.7 mW output power. The LIAD beam was switched on and off with a rate of 5 mHz using an acousto-optic modulator (AOM). This low frequency was chosen in order to test, on which timescale steady state conditions can be reached, to perform experiments at LIAD enhanced high optical densities. Absorption spectra were taken with a rate of about 100 mHz scanning the probe laser in the vicinity of the D1 line. The data was fitted with a gaussian profile and the values for the optical depth was denoted for the transition from the $6S_{1/2} F = 3$ to the $6P_{1/2} F = 4$ state, as this is the one also used for the three photon spectroscopy. All optical depth values arising from spectra taken within one second were averaged and are plotted in figure 13.

A huge increase in the optical depth can be seen when the LIAD beam is switched on. The optical depth reaches values of more than $OD_{max} = 42$, whereas the background value is around $OD_0 = 0.7$. During the time the LIAD pulse is on the optical depth decreases. This can be addressed to atoms diffusing out of the fiber. The timescale does not exactly fit the values calculated in section 5, but is in the same order of magnitude. Considering the first pulse, a kink can be observed during the rise of the optical depth. The origin of this kink is not understood yet. However, experiments which have been reported in [17] show a similar behavior and do also not provide an explanation.

For the three photon excitation, the light at 780 nm is typically used with comparable intensities to the values used here. To get reliable results, the vapor pressure has to be constant during the measurement. However, the conditions are not stable when the beam is switched on. The measurement shown in figure 14 was done in order to investigate how long one has to wait after switching on the LIAD beam until the vapor pressure reaches a new equilibrium. Same as in figure 13, a huge increase in the optical depth can be observed when the LIAD beam is switched on. In figure 14, the optical depth of the system decreases by about one order of magnitude within the first one hour. In order to provide stable conditions, we decided to let the LIAD light switched on for about twelve hours before performing the three photon spectroscopy.

By plotting the data shown in figure 14 on a logarithmic scale, we were not able to assign a simple power law. Assuming the process is dominated by the diffusion out of the fiber, it should match the timescale for the diffusion into the fiber shown in figure 12, which is not the case. The reason for this is the increased desorption (and therefore decrease in the time of adsorption τ) due to the desorption light shone in. A model of LIAD is discussed in [44], introducing a diffusion coefficient at the boundary depending on the wavelength and intensity of the desorption beam and applied for LIAD in macroscopic cells with siloxane coated walls.

On the timescale, considered in figure 13, the switching of the optical depth seems to happen instantaneously. In [45], switching times in the order of $10 \mu\text{s}$ were shown in rubidium vapor inside a hollow core fiber with a diameter of $6 \mu\text{m}$. In order

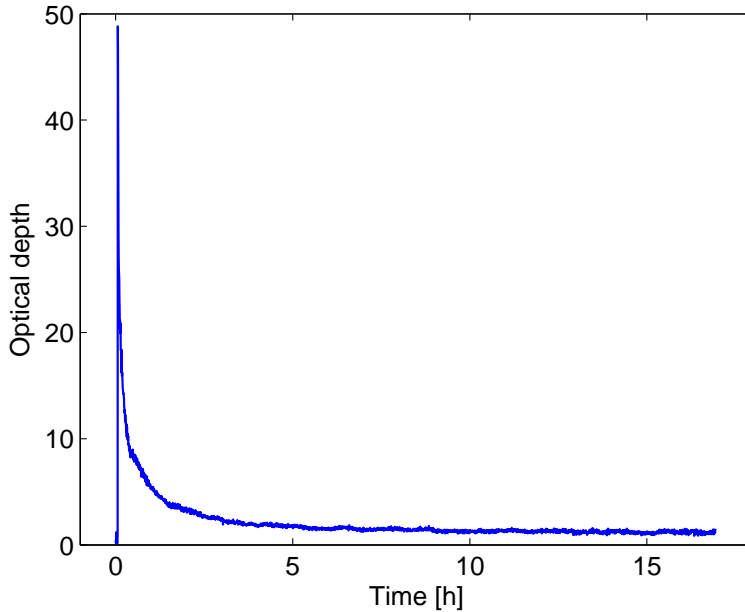


Fig. 14: Change in the optical depth in the HC-PCF with 19 μm core size after switching on the desorption light. Decrease of the optical depth due to diffusion of atoms out of the fiber. The beam powers were set to $P_{\text{P}} = 0.5 \mu\text{W}$ and $P_{\text{LIAD}} = 20 \text{ mW}$.

to figure out whether all-optical switching of a probe beam resonant with the D1 transition can be realized, the timescale of the increase and decrease in atomic density in our system was measured. The probe laser was frequency stabilized on resonance and its transmission recorded on a photodiode. The switching frequency of the desorption pulses was increased until the change in transmission did not follow the switching process anymore. For the switching of the LIAD light, it was ensured that the rise time of the AOM was significantly shorter than the switching period.

In figure 15, the change in the on-resonance transmission (blue) is shown as well as the on and off phases of the desorption beam (green). The beam power of the LIAD beam was raised to $P_{\text{LIAD}} = 63 \text{ mW}$. At the switching frequency of 100 Hz the changes in the transmission does not follow directly anymore. However, this change is a lot slower than the one shown in [45]. We assume that the process shown there is dominated by light induced atomic desorption, where the energy of the photon provides the energy needed to overcome the rubidium quartz binding energy. In contrast, the change in optical density in our system seems to be dominated by surface-plasmon-induced desorption. As this process can be seen as a heating of the cesium clusters, the time needed until the optical density changes is significantly longer than for LIAD.

For the measurements reported in section 7.2, the coupling beam was modulated

6 Measurements on Light Induced Atomic Desorption

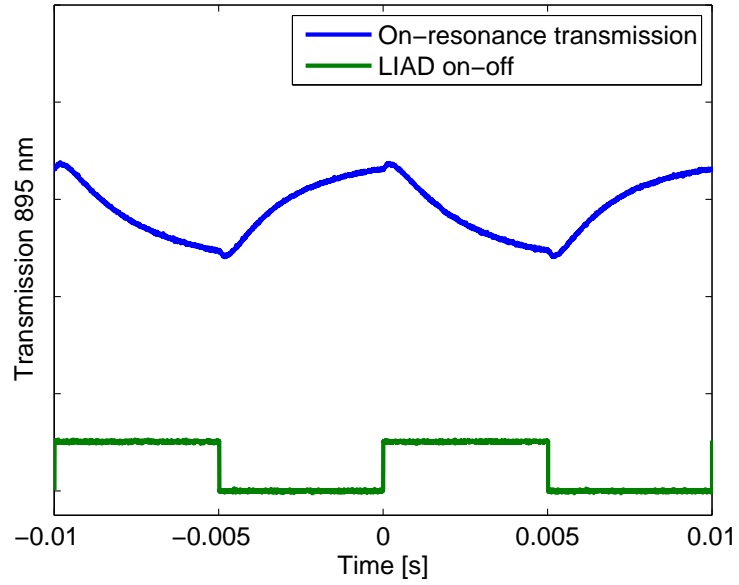


Fig. 15: Change in the optical depth in the HC-PCF with $19\ \mu\text{m}$ core size for desorption pulses of 5 ms. The beam powers were set to $P_P = 0.5\ \mu\text{W}$ and $P_{\text{LIAD}} = 63\ \text{mW}$.

by an AOM with a frequency of 50 kHz to improve the performance of the lock-in amplifier. According to the data shown in figure 15, the optical depth in the system is not modulated at that frequency.

7 Rydberg Spectroscopy

A three photon Rydberg excitation is performed to demonstrate the general feasibility of exciting Rydberg atoms in hollow core fibers. Possible influences of the confinement were studied by comparing spectra measured in various fibers and in a reference cell. Systematic data was taken for a series of Rydberg states with several main quantum numbers from $n = 26$ to $n = 46$.

7.1 Spectra in Kagomé HC-PCF with low Optical Depth

Rydberg excitation in a hot vapor inside a wedge cell ([8]) has shown that the influences of the confinement lead to line shifts and broadenings by atom wall interactions. There, interactions between atoms and close-by walls become relevant for cell thicknesses in the order of $20\ \mu\text{m}$ and increase for higher main quantum numbers as well as for smaller cell thickness. In order to demonstrate whether Rydberg excitation is possible inside a hollow core fiber, we chose the kagomé hollow core photonic crystal fiber with a core size of $60\ \mu\text{m}$ for the first measurements to avoid strong atom wall interactions.

As described in section 4, both the probe and the intermediate laser were locked on resonance. The transmission of the probe beam was recorded, depending on the frequency detuning of the coupling light which was scanning in the vicinity of the Rydberg transition frequency. In figure 16, transmission spectra of the reference cell (green) and the kagomé HC-PCF (blue) are shown, which were taken simultaneously. The input powers for the fiber were set to $P_P = 0.15\ \mu\text{W}$, $P_I = 7\ \mu\text{W}$ and $P_C = 70\ \text{mW}$. As already mentioned in section 4.4, $\approx 40\%$ (895 nm), $\approx 30\%$ (1359 nm) and $\approx 60\%$ (790 nm) of the input power was transmitted through the fiber. For the reference cell, the power values were $P_P = 2\ \mu\text{W}$, $P_I = 200\ \mu\text{W}$ and $P_C = 20\ \text{mW}$ with the $1/e^2$ beam waists given by $w_P = 41.1(10)\ \mu\text{m}$, $w_I = 64.3(12)\ \mu\text{m}$ and $w_C = 46.3(16)\ \mu\text{m}$.

To achieve a better signal to noise ratio, the intermediate laser was amplitude modulated by a chopping wheel with a frequency of 1.1 kHz and the probe transmission signal from the photodiode¹ was processed by a lock-in amplifier². The Rydberg coupling laser was scanned over a range of approximately 1 GHz with a frequency of $f \approx 0.5\ \text{Hz}$, to achieve a significant difference between the timescales of the chopping wheel modulation and the frequency scan. At the same time, the time for the

¹Thorlabs PDA 36A (50 dB)

²Stanford Research Systems Model SR830 DSP, DC coupled

7 Rydberg Spectroscopy

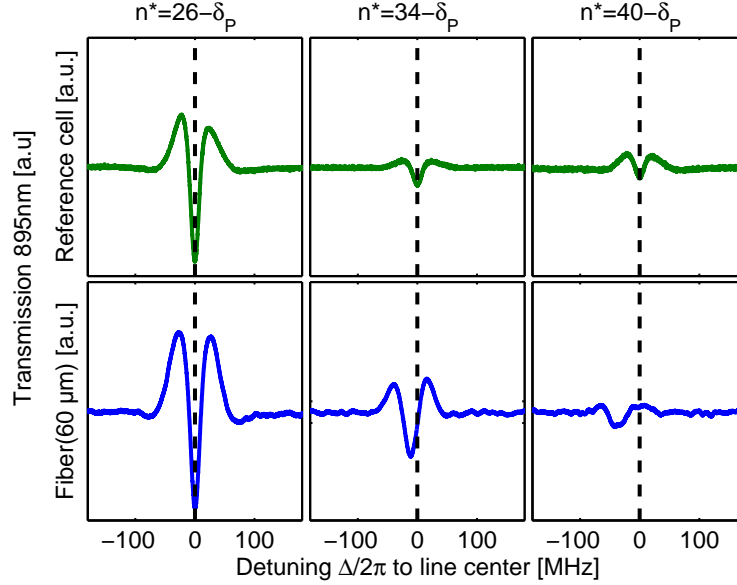


Fig. 16: Transmission of the probe beam with respect to the detuning of the coupling light taken in both the reference cell and the kagomé hollow core photonic crystal fiber with a core size of 60 μm . Exemplarily, spectra for three main quantum numbers is shown. Zero detuning is set to the center of the reference signal and marked by a dashes line. The optical depth of the system was $OD = 0.4$.

measurement procedure was kept within a reasonable length. The lock-in amplifier was operated using an integration time of 3 ms ($\cong 333$ Hz) with a suppression of higher frequency contributions by 18 dB. The output delay due to the integration time obtained 8.2(25) ms. The resulting spectra were averaged over 250 sweeps. The fibers were kept at room temperature and the Rydberg coupling light was shone in for half a day in advance with constant power to get a stable vapor pressure inside the fiber according to the argument in section 6.

The data set shown in figure 16 was taken after two months of exposure of the fibers to the cesium atmosphere. The values for the optical depth were measured with the method explained in 4.5 and resulted in $OD = 0.4$ ($OD_{\text{cladd}} = 0.028$ and $OD_{\text{tot}} = 0.41$).

The frequency axis of figure 16 is scaled using a Fabry-Perot interferometer (see section 4.2). The absorptive dip in the transmission spectrum of the reference cell is fitted by a parabola. The center position of this function is set to zero detuning.

Rydberg states of type $nP_{3/2}$ have been addressed, as the dipole matrix element for the transition from the $7S_{1/2}$ to the $nP_{3/2}$ Rydberg states is larger than to the $nP_{1/2}$ Rydberg states, resulting in a larger signal amplitude. The wavelengths for these transitions are listed in appendix B.

In figure 16 (left), the linewidth of the signal recorded in the fiber are not signif-

7.1 Spectra in Kagomé HC-PCF with low Optical Depth

icantly larger than in the reference for the main quantum number $n = 26$. As the Rydberg atom gets more sensitive to atom wall interaction, fields or other influences for higher main quantum numbers n , the spectra were taken several times, addressing different $nP_{3/2}$ states. For higher main quantum numbers as $n = 34$ (center) and $n = 40$ (right), shown in figure 16, the signal gets significantly broadened, shifted and its amplitude decreases, compared to the spectra taken in the reference cell. However, even for high main quantum numbers, the signal width stays well below the Doppler width ($\omega_D \approx 360$ MHz), which is the benchmark for coherent spectra in thermal vapor. The power of the Rydberg coupling beam was kept constant for all main quantum numbers addressed, to avoid variations in the optical depth due to changing LIAD processes. Hence, the signal strength was decreasing according to the decrease by $\propto (n^*)^{-3/2}$ in the dipole matrix element. However, the decrease in the amplitude of the signal inside the fiber seems to be enhanced in comparison to the reference cell. In order to determine this decrease in a quantitative way, one would need to fit a theoretical curve to the experimental data, which is discussed in section 8.2 in more detail.

After it has been shown that Rydberg excitation is possible in kagomé HC-PCF with a core size of $60 \mu\text{m}$, it is interesting whether this is also possible in fibers with a much smaller core size. Decreasing the core size is of interest, as it will increase the ratio of blockade radius to core radius, for a given main quantum number. If coherence in the system is destroyed by the interactions with the walls, it will increasingly occur for smaller fiber sizes, which requires a closer look on atom wall interactions in such systems.

In figure 17, spectra obtained in the fiber with $19 \mu\text{m}$ core size are shown. All technical steps to obtain the signal such as scaling of the frequency axis etc., are the same as for the data shown in figure 16. The number of averages was decreased to 100 spectra for figure 17 instead of 250. The beam powers in front of the fiber were $P_P = 0.3 \mu\text{W}$, $P_I = 6 \mu\text{W}$ and $P_C = 50 \text{mW}$. The transmission of the incoupled light power was in the order of $\approx 30 \%$ (895 nm), $\approx 20 \%$ (1359 nm) and $\approx 40 \%$ (790 nm).

For the reference cell, the input powers for $n = 26$ were $P_P = 1 \mu\text{W}$, $P_I = 220 \mu\text{W}$ and $P_C = 20 \text{mW}$. As the power for the reference cell in the Rydberg coupling beam was not adjusted after changing the main quantum number, the signal size increases for higher main quantum numbers due to an increase in the output power of the tapered amplifier.

The signal measured in the fiber (shown in figure 17) is broader than the one measured in the reference cell. Increasing the main quantum number, this broadening increases and for main quantum numbers higher than $n = 30$ no signal can be obtained anymore. In contrast to this, for main quantum numbers of $n = 40$ and even higher, Rydberg excitation was observed in the fiber with $60 \mu\text{m}$ core size. The optical depth values in the fiber were measured to be $OD = 0.2$ ($OD_{\text{cladd}} = 0.016$ and $OD_{\text{tot}} = 0.21$). However, the signal contribution arising from the part in front and behind the fiber is relevant. The spectra show a broadened and shifted signal, as well as a smaller, narrower and unshifted one at resonance. This smaller sig-

7 Rydberg Spectroscopy

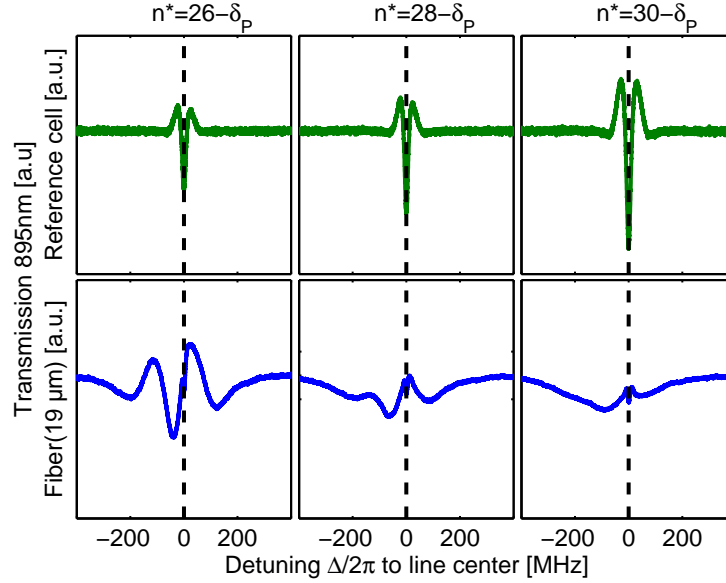


Fig. 17: Transmission of the probe beam with respect to the detuning of the coupling light, taken in both the reference cell and the kagomé HC-PCF with a core size of $19 \mu\text{m}$. The transmission is shown exemplarily for a set of three main quantum numbers. Zero detuning is set to the center of the reference signal and marked by a dashed line. The optical depth of the system was $OD = 0.2$.

nal is attributed to the absorption in front and behind the fiber, where atom wall interaction does not play a role.

The calculations in section 5 show that a filling time of about 14 h accounts for the core of the $60 \mu\text{m}$ fiber and about 6 d for the one with $19 \mu\text{m}$ core diameter. Therefore, the filling after two months should have exceeded 99 % of the background pressure and the optical depth should have been more than 3, considering the vapor pressure and length of the fiber. No measurements of the optical depth in the vacuum chamber have been performed at that time to determine the background pressure. However, in figure 14 which was measured afterwards, the optical depth falls below $OD = 1.2$ after 15 h. This suggests that the optical depth in the vacuum chamber was below this value as well. This could explain the low optical densities in the fibers. Additionally, some residual background gas could also have led to a broadening of the lines. Collisions with a background gas atoms however, can not be the origin for the frequency shifts observed.

To get a better understanding of how the signal changes with main quantum number, a systematic measurement series was performed in the kagomé HC-PCF with $60 \mu\text{m}$ core diameter, depicted in figure 18. An increasing shift with respect to the reference cell and the enhanced broadening for higher main quantum numbers can be observed.

7.1 Spectra in Kagomé HC-PCF with low Optical Depth

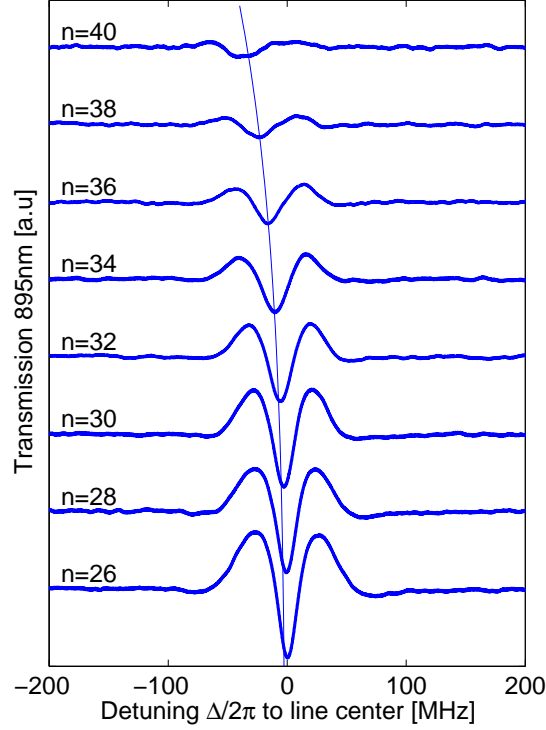


Fig. 18: Transmission of the probe laser with respect to the detuning of the coupling laser measured in the kagomé hollow core photonic crystal fiber with a core size of $60 \mu\text{m}$. The data is shown for a set of main quantum numbers for $OD = 0.4$. The power law fitted to the line shifts is depicted.

The origin of the deviation between fiber and reference signal were investigated by analyzing the line shifts of the signal. The signal positions are less complicated to extract than the amplitude and broadening, which also depend on the excitation strength. In figure 19 the frequency shifts δ with respect to the effective main quantum number n^* are shown, using a double logarithmic scaling in order to compare them to typical scaling laws for Rydberg states. The shift values for the fiber data with respect to the reference cell are obtained by fitting a parabola to the absorptive dip of the transmission spectrum. Error bars on the frequency shift include:

- the uncertainty on the time offset by the lock-in amplifier,
- the uncertainty in scaling the frequency axis with spectrum of the Fabry-Perot interferometer and
- the uncertainties in fitting the line centers.

7 Rydberg Spectroscopy

The shifts can be fitted by a power law, corresponding to a straight line in the double logarithmic plot. The power law found for the shifts observed in the fiber with 60 μm core diameter is

$$\delta_{60\mu\text{m}} = \delta_0 + \delta_1 \cdot (n^*)^\nu \quad (7.1)$$

with the fitted parameters

$$\delta_0 = -1.52(128) \text{ MHz} \quad (7.2)$$

$$\delta_1 = -1.50(330) \times 10^{-9} \text{ MHz} \quad (7.3)$$

$$\nu = 6.67 \pm 0.61. \quad (7.4)$$

The constant offset δ_0 is fitted, as the error in the delay time of the lock-in amplifier was quite large. This large error occurred, as the delay time was first measured by comparing the signal shift for two scan directions of the coupling laser. The second measurement was performed by measuring the time delay between a steep slope given to in input of the lock-in amplifier, with its output. The resulting delay times, obtained by this two methods showed large deviations. Therefore, the values in figure 19 are shifted by the frequency offset δ_0 obtained from the fit.

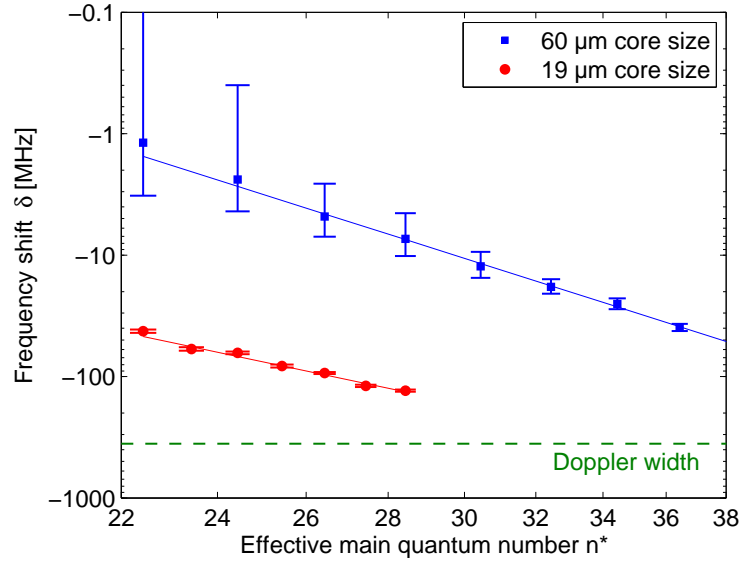


Fig. 19: The relative frequency shift of the spectra measured in both the fiber with 60 μm and 19 μm core size with respect to the reference cell are shown applying a double logarithmic scaling of the axes. All shifts are well below the Doppler width. The spectra evaluated to obtain the shift values, are presented in appendix C. The frequency shifts are fitted according to equation 7.1 and equation 7.6.

7.1 Spectra in Kagomé HC-PCF with low Optical Depth

It is conspicuous that the scaling law has an exponent ν close to 7, which matches the scaling of the polarizability with respect to the main quantum number as mentioned in section 2.2. The DC Stark effect, explained in section 2.3, leads to line shifts of

$$\delta = \frac{1}{2}\alpha_P E^2 \quad (7.5)$$

with the polarizability $\alpha_P \propto (n^*)^7$. Using the polarizability values of [27], one could assign the line shifts observed in the experiment to static electric fields with a field strength of about $E \approx 0.5 \text{ V cm}^{-1}$. This is a astonishing result, as the lines in 18 seem to be only shifted but show very few asymmetric broadening at the same time. One could therefore assume that the field causing the shift is rather homogeneous. However, the field strength of about $E \approx 0.5 \text{ V cm}^{-1}$, is low. To achieve such low electric field values, only very few single charges on the surface of the fiber core wall would already be sufficient. This should lead to a very inhomogeneous field distribution. It seems to be more plausible that - if the line shifts are caused by an electric field - the source of the field was located outside the fiber e.g. on the glass jacket of the fiber.

The line shifts observed in the fiber with $19 \mu\text{m}$ core size are significantly larger than the ones of the $60 \mu\text{m}$ core. Fitting a power law to the frequency shifts observed in the $19 \mu\text{m}$ fiber resulted in

$$\delta_{19 \mu\text{m}} = \delta_1 \cdot (n^*)^\nu \quad (7.6)$$

with the fitted parameters

$$\delta_1 = -4.95(546) \times 10^{-5} \text{ MHz} \quad (7.7)$$

$$\nu = 4.42 \pm 0.33. \quad (7.8)$$

No constant offset was fitted, but the offset δ_0 - which is assigned to the delay of the lock-in amplifier - is taken from the fit of the data in the fiber with $60 \mu\text{m}$ core size. As the scaling is quite different to well-known scaling laws for Rydberg atoms, it is not clear what effects contributed to these shift and broadening of the atomic lines. Considering electric fields as one possible reason for the line shifts in the fiber with the larger core diameter, inhomogeneous electric fields could contribute to the line shifts and broadening in the fiber with $19 \mu\text{m}$ core diameter.

One could think that the broadening of the lines arises from the limited lifetime of the Rydberg atoms, as they “crash” into the wall of the fiber promptly. This transit time broadening amounts to about 4.9 MHz for the fiber with $19 \mu\text{m}$ core size and is therefore clearly smaller than the scale of the broadened signal. For smaller core sizes which might be studied in future experiments, this broadening mechanism will become more important. In comparison to this, the transit time broadening for the fiber with $60 \mu\text{m}$ is 1.5 MHz and 0.7 MHz for the reference cell.

7.2 Spectra in Kagomé HC-PCF with high Optical Depth

After these measurements, the LIAD measurements discussed in section 6 were performed. The results presented there demonstrate that modulation of the coupling beam via an AOM can increase the performance of the lock-in amplifier but does not modulate the optical depth in the system, as long as the modulation is performed fast enough. Therefore, the setup was changed accordingly.

With this setup, a new series of Rydberg spectroscopy measurements was performed. The resulting spectra are shown together with the previous measurements in figure 20 for the fiber with 60 μm core size. The input powers for the measurement were $P_P = 0.5 \mu\text{W}$, $P_I = 10 \mu\text{W}$ and $P_C = 30 \text{mW}$ for the fiber. This led to fiber output powers of $P_P = 0.2 \mu\text{W}$, $P_I = 2.4 \mu\text{W}$ and $P_C = 14.6 \text{mW}$. For the reference cell, the powers were adjusted to $P_P = 1 \mu\text{W}$, $P_I = 60 \mu\text{W}$ and $P_C = 30 \text{mW}$.

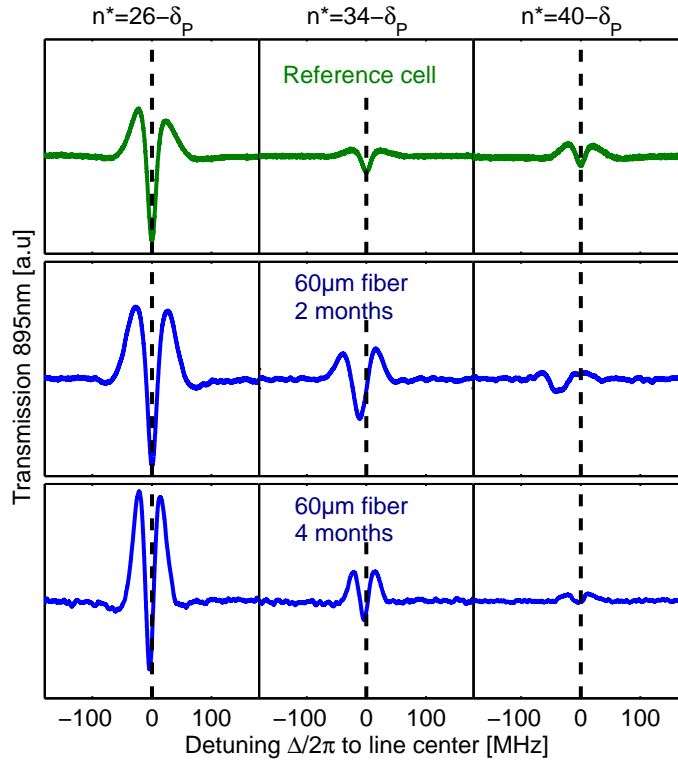


Fig. 20: The transmission of the probe beam is recorded depending on the frequency of the coupling laser. The spectra obtained is shown for the reference cell as well as for the fiber with 60 μm core size for three main quantum numbers. The difference between the signals shown in the second and the third line is the longer exposure time to the cesium atmosphere as well as the higher optical depth of $OD = 3$ in the system for the later measurements.

7.2 Spectra in Kagomé HC-PCF with high Optical Depth

The coupling beam was modulated with a 50 kHz square wave signal and the lock-in amplifier was operated with an integration time of 100 μ s, leading to an output delay of about 400 μ s. Signal contributions faster than this 100 μ s were attenuated by 24 dB. As the modulation is a lot faster compared to the chopping wheel, the scan frequency of the coupling laser was increased to about 2.5 Hz. For main quantum numbers up to $n = 38$ about 200 spectra were averaged and about 350 for main quantum numbers larger than that. Apart from this, the measurement procedure was the same as for previous measurements. The optical depth in the system was measured as described in section 4.5 to $OD = 3$ ($OD_{\text{tot}} = 3.0$ and $OD_{\text{cladd}} = 0.13$). At this time, the optical depth in the chamber outside the fiber was measured as well. This resulted in $OD_{\text{chamber}} = 2.4$. Apparently, the optical depth inside the fiber was even higher than in the chamber.

In figure 20, the transmission of the probe beam with respect to the detuning of the coupling laser is shown for a set of three different main quantum numbers. For comparison, the spectra obtained after four months at an optical depth of $OD = 3$ are shown together with the signal recorded after two months of exposure time ($OD = 0.4$) and the reference cell. Especially for the higher main quantum number, the signal appears narrower in frequency than the one taken after two months. Even more noticeable is that the signal obtained after four months is not shifted with respect to the reference cell signal.

Since the transmission spectra in the fiber with the larger core size exhibit less deviations from the reference cell signal after four months than in the previous measurements, the validation of this effect using the fiber with 19 μ m core size lies at hand. Using the lock-in amplifier the same way as for the other fiber, the spectra shown in figure 21 were taken with laser power values of $P_P = 0.15 \mu$ W, $P_I = 10 \mu$ W and $P_C = 20$ mW for the fiber. For the reference cell the powers were adjusted to $P_P = 1 \mu$ W, $P_I = 60 \mu$ W and $P_C = 20$ mW. The spectra were averaged between 200 and 400 times. The optical depth in the system was $OD = 1.5$ ($OD_{\text{tot}} = 1.54$ and $OD_{\text{cladd}} = 0.08$).

In figure 21, the three photon signal is shown for the reference cell, the fiber after two months of exposure to the cesium atmosphere and the fiber after four months of exposure. Three different main quantum numbers are selected, to shown how the increased sensitivity of the Rydberg atom for higher main quantum numbers influences the signal.

Comparing the transmission spectra taken in the fiber after two months to the ones taken later, a clear decrease of the linewidth can be observed. Even for a main quantum number of $n = 30$, the typical line shape can be seen, where only a broad absorptive dip could be resolved in the measurements after two months. For this measurement, the transit time broadening of 4.9 MHz might already have been one of the limiting factors for the linewidth. The line shifts with respect to the reference cell have vanished almost completely. We address the residual line shifts to technical issues, as the signal with $n = 26$ is shifted already and the exact time delay caused by the lock-in amplifier was not clear.

7 Rydberg Spectroscopy

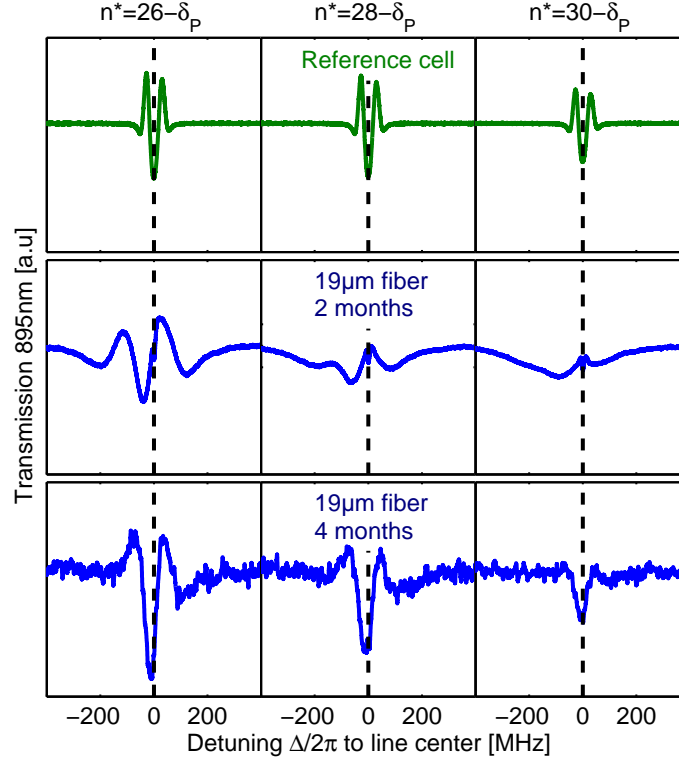


Fig. 21: The transmission of the probe beam is recorded depending on the frequency of the coupling laser. The spectra obtained is shown for the reference cell as well as for the fiber with $19\ \mu\text{m}$ core size for three main quantum numbers. The difference between the signals shown in the second and the third line is the longer exposure time to the cesium atmosphere as well as the higher optical depth of $OD = 1.5$ in the system for the later measurements.

Figure 22 gives an overview of the line shifts observed in the two fibers both after two and four months of exposure time. The line shifts observed in the fiber with $60\ \mu\text{m}$ core diameter are indicated by blue squares, the shifts for the fiber with $19\ \mu\text{m}$ core diameter by red circles. While the filled symbols correspond to the frequency shifts after two months of exposure to the cesium atmosphere, the empty circles correspond to the line shifts of the spectra measured after four months.

The line shifts in the fiber with $19\ \mu\text{m}$ have decreased by about one order of magnitude. The line shifts in both fibers show no dependence on the main quantum number after four months of exposure time, which has been the case after two months. Therefore, the line shifts observed after two months of exposure time are unlikely to be only caused by atom wall interaction, as these mainly depend on the atom wall distance. Therefore, it could not vanish with a change in the optical

7.2 Spectra in Kagomé HC-PCF with high Optical Depth

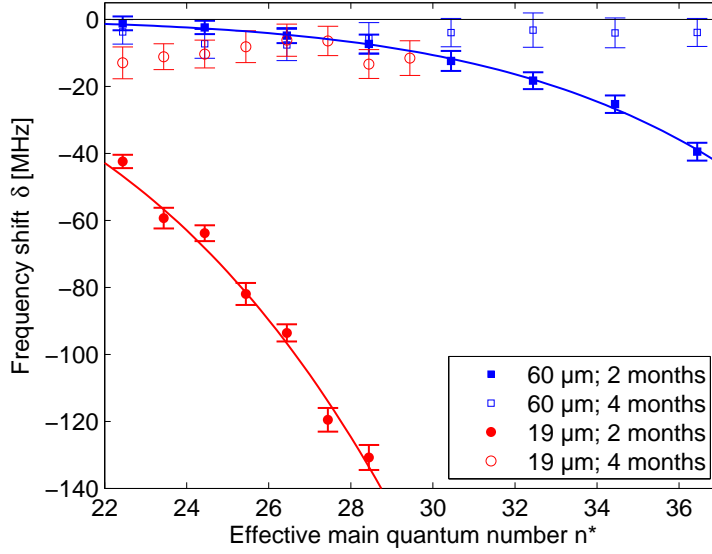


Fig. 22: The relative frequency shift of the spectra measured in the fibers with 60 μm and 19 μm core diameter with respect to the reference cell. Shifts observed after two months (filled symbols) of exposure to the cesium atmosphere have vanished after four months (empty symbols). All spectra evaluated to obtain the shift values, are presented in appendix C.

depth, exposure time and coverage of the wall with cesium.

To assign the origin of the line shift to electric fields is more reasonable, as electric fields could be shielded, when the core walls and the walls of neighboring holes are covered with cesium. Additionally, a cesium layer on the walls could allow charges to flow off. One reason for such charges on the surface or in holes of the fiber could have been that the fiber was rubbed during cleaning before being placed in the vacuum chamber, in order to get rid of residual coating material.

Although, both fiber cores should have reached more than 99% of the vapor pressure in the chamber after two months, according to the calculations in 5, this does not account for the small triangular holes in the photonic crystal structure of the fiber. At room temperature, the calculations from section 5 result in a filling fraction of $\approx 55\%$ after two months and $\approx 87\%$ after four months for the triangular holes³ of the fiber with 60 μm diameter. For the triangular holes in the photonic crystal structure of the 19 μm fiber, the filling fraction is $\approx 33\%$ after two months and $\approx 65\%$ after four months. One could conclude that not only a uniform coverage of the inner core walls, but also of the surrounding walls of the photonic crystal structure is needed to prevent the Rydberg atoms effectively from line shifts caused by electric

³The area preserving radius given in table 4.1 was used for the diffusion calculations.

fields. Increased heating of the fiber after exposure to the cesium atmosphere could have speeded up the filling process, as the time of adsorption is decreased for higher wall temperature.

Apart from this, between the measurement series taken after two months and the one taken after four months, the valve to the vacuum pump was opened for a few hours. If there was some background gas present at the measurements done after two months, this should have vanished during this pumping time. Afterwards, the chamber was slightly heated for a couple of days. It might be, that this has led to an increased number density inside the vacuum chamber.

7.3 Spectra in 70 μm Capillary

In order to study atom wall interactions, the comparison between kagomé HC-PCF and capillaries can be instructive, as the core walls of the kagomé HC-PCF are only a few hundred nanometers thick, whereas the capillary walls show thicknesses of several hundred micrometer. One could learn whether the interaction depends strongly on the thickness of the material or effects related to the surface coverage and mirror charges are dominant. Measurements in a capillary with a core diameter of 70 μm were performed, to check, whether Rydberg excitation is in general possible in capillaries. The atom wall interactions are expected to be negligible for this large diameter.

The incoupling beam powers were adjusted to $P_P = 1 \mu\text{W}$, $P_I = 40 \mu\text{W}$ and $P_C = 40 \text{mW}$. The transmission was $\approx 8\%$ for the intermediate laser and $\approx 40\%$ for the coupling laser. The output power of the probe beam was not measured, but we estimate the transmission of the probe beam to be about $10\% - 20\%$ of the input power. The measurements were performed after the fiber was exposed to the cesium atmosphere for four months. The calculated filling time for the fiber is 12 h (see section 5). Measurements on the optical depth of the system resulted in $OD \approx 1.6$ ($OD_{\text{tot}} \approx 1.8$ and $OD_{\text{cladd}} = 0.14$). The optical depth in the chamber was measured a few days later to be $OD_{\text{chamber}} = 1.5$.

Analogously to the measurements performed in the kagomé HC-PCF, the main quantum number of the Rydberg state was increased systematically, to see whether new effects show up for the higher polarizabilities. In figure 23, the corresponding spectra are shown. These spectra were averaged 200 times. For the ones with $n = 44$ and $n = 46$ the data was averaged over 600 samples. One can observe, that the signal widths are comparable to the ones in the kagomé HC-PCF with 60 μm core diameter. As for the kagomé HC-PCF, the spectra get broader for higher main quantum number.

In figure 23, zero detuning is indicated by a black dashed line. A small offset shift of the Rydberg lines can be read off, which might be caused by technical issues. No line shift depending on the main quantum number of the Rydberg state addressed can be seen. The highest quantum number for which a three photon transmission

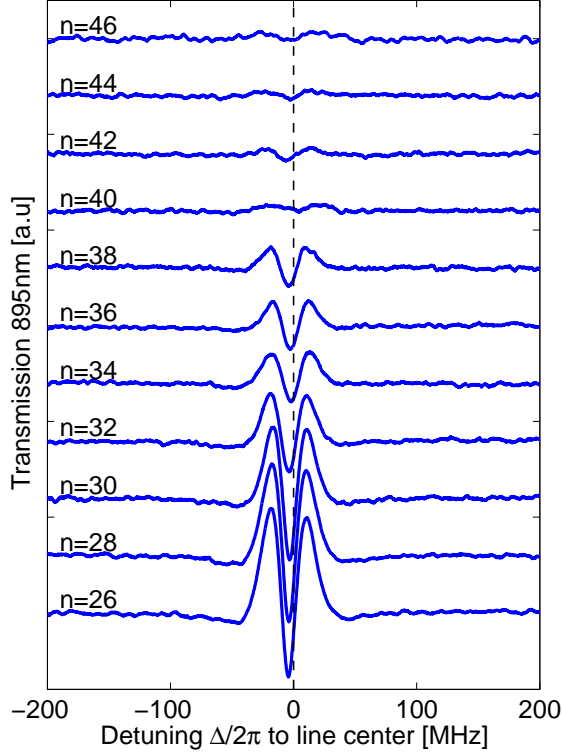


Fig. 23: Transmission of the probe laser with respect to the detuning of the coupling laser measured in the capillary with a core diameter of $70 \mu\text{m}$. The data is shown for a set of main quantum numbers for $OD \approx 1.6$. Zero detuning is set to the center of the reference signal. The incoupling powers were set to $P_P = 1 \mu\text{W}$, $P_I = 40 \mu\text{W}$ and $P_C = 40 \text{mW}$.

spectrum could be observed was $n = 46$. This indicates a vanishing influence of capillary on the Rydberg lines of the atoms confined.

7.4 Off-resonant Rydberg Excitation

Electromagnetically induced transparency (EIT) performed on Rydberg atoms inside single mode hollow core fibers could be a suitable system to create slow light or even non-classical light via Rydberg-Rydberg interaction. To do so, the excitation scheme applied in the previous measurements is not suited, as an absorptive dip appears when the coupling beam is on resonance. For the generation of slow light or non-classical light, one requires enhanced on-resonance transmission. Additionally, the three level EIT scheme is theoretically more feasible to analyze than the four

7 Rydberg Spectroscopy

level system applied in this work. Therefore, it might be easier to fit a theoretical model to the experimental data.

In order to get an effective three level system, the intermediate laser is now frequency stabilized with an offset of -400 MHz to the $6P_{1/2}$ to $7S_{1/2}$ transition, well beyond the Doppler width, as shown in figure 24. This frequency offset is realized by the two AOMs in the setup, shown in section 6, each shifting the frequency by 100 MHz and both passed two times. This leads to an off-resonant two photon absorption of the intermediate and coupling light, when the three photon spectroscopy is performed. As those two photons only get absorbed together, the excitation to the

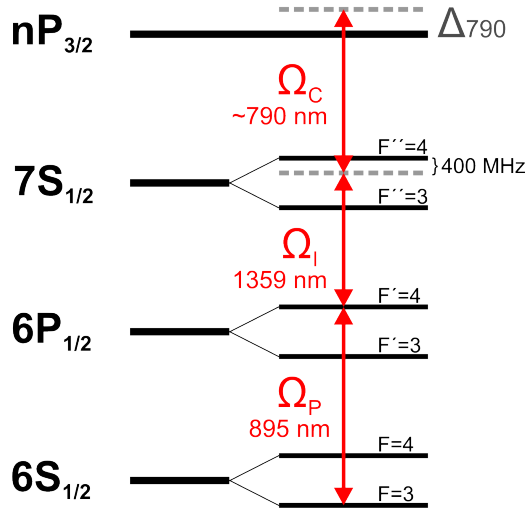


Fig. 24: Excitation scheme for the off-resonant spectroscopy. The probe laser is frequency stabilized on resonance, the intermediate laser is stabilized 400 MHz below the resonance frequency of the intermediate transition and the coupling laser is scanning in the vicinity of the transition to the Rydberg state.

Rydberg state effectively is a standard EIT configuration with the probe transition at 895 nm having a longer wavelength than the effective wavelength of the transition from the $6P_{1/2}$ to the Rydberg state.

To test the system, the $26P_{3/2}$ Rydberg state was addressed and the laser powers were adjusted to $P_P = 1 \mu\text{W}$, $P_I = 3 \text{ mW}$ and $P_C = 43 \text{ mW}$ in front of the kagomé HC-PCF with $60 \mu\text{m}$ core diameter. For the reference cell the beam powers were set to $P_P = 1 \mu\text{W}$, $P_I = 2 \text{ mW}$ and $P_C = 8.2 \text{ mW}$. The optical depth in the fiber was measured to be $OD \approx 0.15$ ($OD_{tot} \approx 0.22$ and $OD_{cladd} = 0.07$). For the $26P_{3/2}$ state the coupling strength is large in comparison to the coupling strength to Rydberg states with higher main quantum number, which results in a reasonable signal amplitude. Therefore, no lock-in amplifier was used, in order to avoid the uncertainties caused by the large error in the lock-in amplifier delay time⁴.

⁴Two new identical lock-in amplifiers were ordered to measure both the fiber and the reference

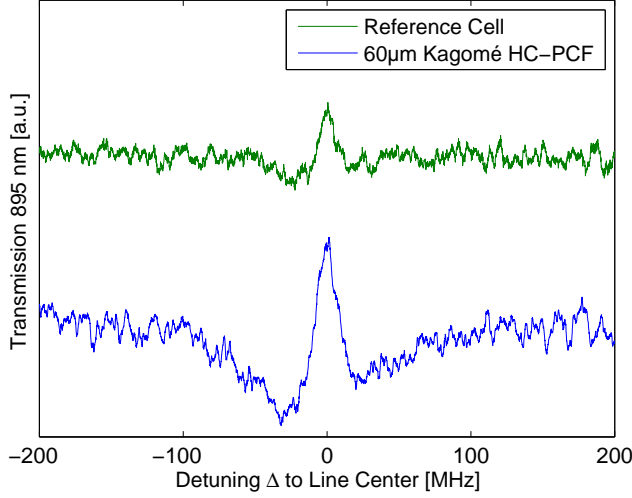


Fig. 25: The transmission of the probe laser is shown depending on the detuning of the coupling laser to resonance. The intermediate laser was frequency stabilized -400 MHz off-resonant. The spectrum is shown for the reference cell (green) and the kagomé HC-PCF with $60\ \mu\text{m}$ core diameter (blue), taken simultaneously. The beam powers were set to $P_P = 1\ \mu\text{W}$, $P_I = 3\ \text{mW}$ and $P_C = 43\ \text{mW}$ in front of the fiber and to $P_P = 1\ \mu\text{W}$, $P_I = 2\ \text{mW}$ and $P_C = 8.2\ \text{mW}$ for the reference cell.

In figure 25 the probe transmission spectrum depending on the detuning of the coupling laser can be seen for an off-resonantly frequency stabilized intermediate laser. The spectrum is shown for both the reference cell (green) and the kagomé HC-PCF with a core diameter of $60\ \mu\text{m}$ (blue). One can see, that it is in principal possible to off-resonantly excite Rydberg atoms inside the fiber. The spectra shown in figure 25 was a first try and the parameters were not optimized. It is not clear, whether the frequency broadening of the fiber spectrum is due to power broadening, background gas or caused by the confinement.

However, at this point, technical issues with the vacuum system occurred, which maybe have influenced the measurement shown in figure 25 already. Due to this, no further measurements on the off-resonant absorption could be performed to systematically investigate this system.

spectrum with the same system having the exact same delay times.

8 Simulation of the Four Level System

The theoretical model applied to simulate the transmission spectra is presented in this chapter. First, the general approach is briefly explained and then both the influence of the Doppler effect and the Gaussian beam shape is discussed in more detail. Finally, the model is fitted to one of the measured spectra.

8.1 Model

For the measurements performed in this work, the excitation scheme shown in section 4.2 was applied. The transmission of the frequency stabilized probe laser was detected depending on the frequency detuning of the Rydberg laser with respect to the resonance frequency. The intermediate laser was frequency stabilized as well and both the intermediate and the Rydberg laser were passing the medium in the opposite direction with respect to the probe laser.

To calculate the transmission signal of the probe laser, the steady state solution $\dot{\rho} = 0$ of the Lindblad equation (equation 2.3) with the Hamiltonian (equation 2.31) including the Lindblad operator (equation 2.32) is searched for. This leads to a system of 16 coupled linear equations which has to be solved under the assumption that the trace of the density matrix equals one:

$$\text{tr}(\rho) = \rho_{11} + \rho_{22} + \rho_{33} + \rho_{44} \stackrel{!}{=} 1. \quad (8.1)$$

By solving the set of equations, the density matrix element ρ_{21} is obtained. The optical depth in the system scales linear with this density matrix element as discussed in section 2.1.3. To obtain the final transmission values t , the prefactor amp for this linear scaling is introduced in the model by

$$t = V_{\text{fos}} \cdot e^{amp \cdot \rho_{21}}, \quad (8.2)$$

as well as the scaling factor V_{fos} . These parameters will be used to scale the theoretical signal to the voltage measured on the photodiode.

As both the probe laser and the intermediate laser are frequency stabilized on resonance, the detuning values Δ_{12} and Δ_{23} in the Hamilton operator are set to zero. The Rabi frequencies in the Hamilton operator are calculated using equation 2.10 with the transition dipole matrix elements and decay rates given in appendix A.

To include the Doppler effect, this system is solved for a set of different velocity classes and the results are weighted by the Boltzmann factor. In figure 26, the result

8 Simulation of the Four Level System

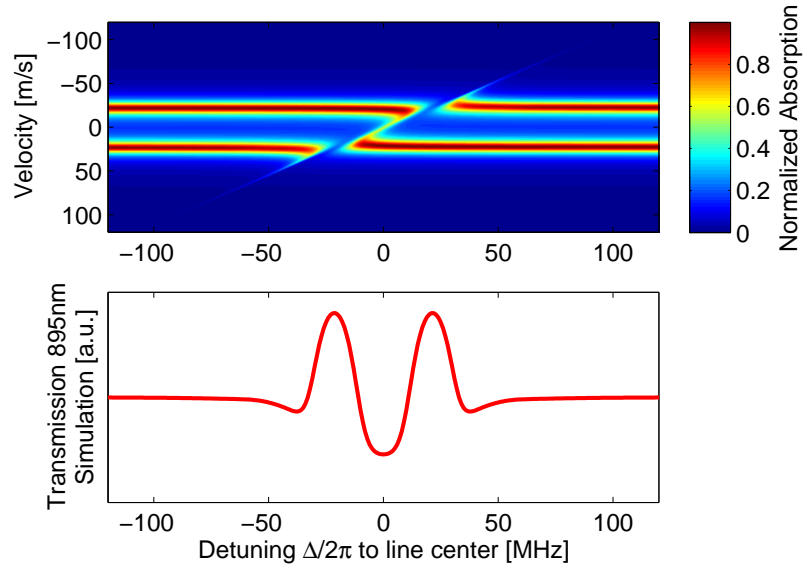


Fig. 26: Example of the simulation signal obtained by finding the steady state solution of the Lindblad equation. In the upper plot, the absorption of the probe laser is shown, depending on the velocity of the atom and the detuning of the Rydberg laser with respect to the resonance frequency. The lower plot shows the resulting transmission spectrum when summing up the contributions of all velocity classes. ($T = 296$ K, $\Omega_{12} = 2\pi \times 8$ MHz, $\Omega_{23} = 2\pi \times 30$ MHz and $\Omega_{34} = 2\pi \times 10$ MHz)

of such a simulation is shown for a temperature of $T = 296$ K and Rabi frequencies of $\Omega_{12} = 2\pi \times 8$ MHz, $\Omega_{23} = 2\pi \times 30$ MHz and $\Omega_{34} = 2\pi \times 10$ MHz. In the upper plot of figure 26, the absorption depending on the detuning of the Rydberg laser is shown for different velocity classes. The lower plot shows how this contributions add up to the total transmission signal. In [46], the transmission as a function of the velocity is discussed, which also depends on the ratio between the intermediate and the coupling laser intensities.

The strength of the atom light coupling in the model is given by the three rabi frequencies. In equation 2.10, the Rabi frequency is related to the intensity of the light field. The power of the beam and the beam waist are measured in the experiment and with this, the intensity distribution can be calculated using equation 2.28. It turns out that the line shape of the simulation can not fit the experimental spectra in a satisfying way, when only one set of Rabi frequencies is taken into account. Therefore, the Gaussian beam profile needs to be included into the calculations. For the purpose of not scaling up the computing time too much, the radial discretization of the Gaussian intensity profile was not distributed linearly. Instead, the Gaussian beam profile was split radially in a way, that each part contributed the same light power on the detector. Hence, the power a of every part was calculated by dividing

the total power up to a cutoff radius r_{max} by the number of areas m , by

$$\frac{a}{I_0} = \frac{2\pi}{m} \int_0^{r_{max}} e^{-2r^2/w_0^2} r \, dr = \frac{\pi w_0^2}{2m} \left(1 - e^{-2r_{max}^2/w_0^2}\right). \quad (8.3)$$

For the case of five divisions $m = 5$ and a beam waist of $w_0 = 19.2 \mu\text{m}$ the right plot of figure 27 shows exemplarily the discretization of the intensity profile.

As the power is given by the product of the area and the intensity, there is a trade-off, as the intensity decreases away from the center of the beam, but the ring area increases for constant radial thicknesses. In the middle of the beam, the intensity is at its maximum, but the geometric area is quite small in comparison to the total area illuminated on the photodiode. Therefore, the range of radii r values for the most inner (dark blue) area is larger than for the following areas (green, red and cyan). Far away from the beam center, the intensity of the beam is relatively low and the increase of the ring area can not completely compensate for that. This leads to a larger range of radii covered by the outmost part (purple).

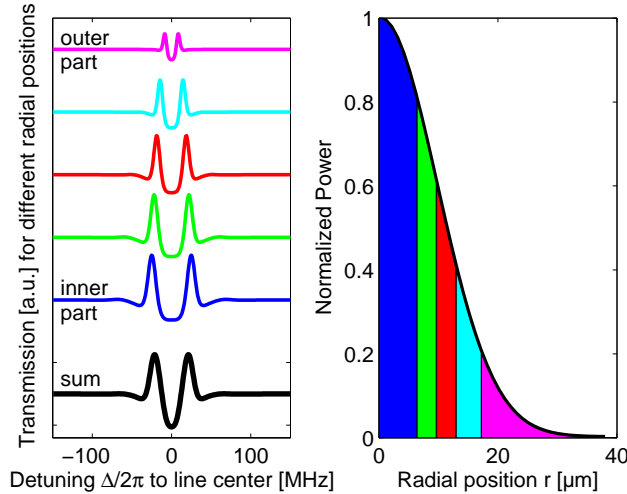


Fig. 27: The changes in the transmission spectrum for different radial positions from the beam center are shown in the left plot. The black line shows the total absorption for taking all contributions into account. The right plot shows which range of radii of the gaussian beam profile contribute to which of the absorption spectra¹.

For the three light fields, three Rabi frequencies need to be assigned to each radial division of the beam. Each of the radial parts contributes the same power to the

¹Values: $P_P = 200 \text{ nW}$, $P_I = 2.4 \mu\text{W}$, $P_C = 14.6 \text{ mW}$, $r_{max} = 2 w_0$, $T = 296 \text{ K}$, $\Gamma_{41} = 0.9 \text{ MHz}$, $n = 30$ and the scaling constants $V_{fos} = 1.7e5$, $amp = 580$. The beam waist was set to $w_0 = 19.2 \mu\text{m}$, which is the the beam waist corresponding to the flat-to-flat radius in the $60 \mu\text{m}$ core fiber.

8 Simulation of the Four Level System

measured signal and the Rabi frequencies were calculated at the radial position r_j of each division, where half of the power a is contributed from larger radial values and half of it from smaller ones. One could say that these radial discretization values are each power-wise in the middle of their division. In order to find this radius r_j values, equation 8.3 was rearranged to

$$r_j = \sqrt{\frac{w_0^2}{2} \left| \ln \left(1 - (2j - 1) \frac{a}{I_0 w_0^2 \pi} \right) \right|}. \quad (8.4)$$

The transmission is then calculated for the intensities (and therefore different Rabi frequencies) at all radial positions r_j , added up and divided by the number m of areas taken into account. In the left plot of figure 27, the contributions from the different parts of the Gaussian beam are shown in the corresponding color. The black transmission curve is the sum of all these contributions.

Typically, good results can be achieved by setting $m \geq 15$ and $r_{max} \geq 2w_0$. When the Gaussian beam shape is included in the simulation, signals calculated for various Rabi frequencies are summed up. Therefore, no specific Rabi frequency can be assigned to the spectrum anymore. The power values for the beams and the beam waist need to be given. To get an idea of the magnitude of the Rabi frequencies, one can refer to the peak Rabi frequencies.

8.2 Fitting the Model to the Experimental Data

The best fit between theoretical and experimental spectrum that could be achieved is shown in figure 28. For both the experiment and the theoretical calculations, the main quantum number was $n = 30$, the beam waist for the beams inside the fiber was $w_0 = 0.64 \times 30 \mu\text{m} = 19.2 \mu\text{m}$ and the temperature $T = 296 \text{ K}$. In the experiment, the outcoupled beam powers from the fiber were measured to be $P_P = 0.2 \mu\text{W}$, $P_I = 2.4 \mu\text{W}$ and $P_C = 14.6 \text{ mW}$.

As the simulated signal shape for this parameters has shown strong deviations to the measured signal, only the beam power values of the probe and the intermediate laser were fixed in the theory. For the theory curve in figure 28, the fitted coupling intensity was $P_C = 201(8) \text{ mW}$. Other parameters which fitted, have been the effective decay rate $\Gamma_{41} = 0.90(3) \text{ MHz}$ for the decay from the Rydberg state to the ground state of the atoms as well as the amplitude $amp = 1.71(4) \times 10^5$ and the scaling factor $V_{fos} = 580 \pm 53$. Even if the line shape seems to be nicely reproducible with the theory, fixing the scaling factors and trying to fit the theory to the experimental data for other main quantum numbers failed. These factors should not change from one measurement to the next within one data set.

One possible explanation could be that the change in the Rydberg coupling strength for different main quantum numbers addressed leads to variations of the optical pumping in the system. The deviations between theory and experiment show that the model needs to be extended to fully describe the system. For example, the

8.2 Fitting the Model to the Experimental Data

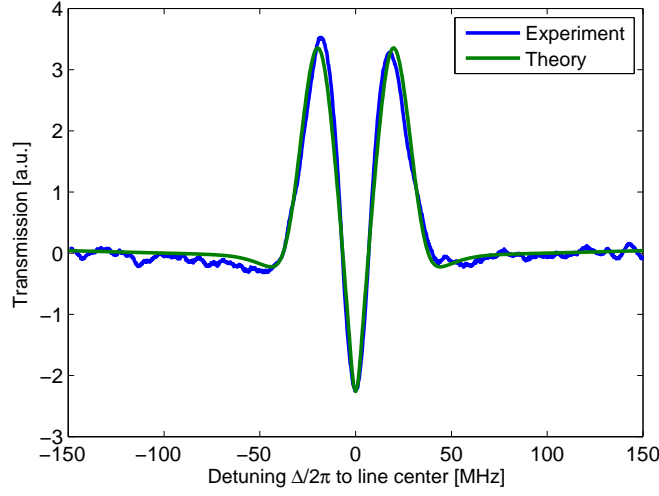


Fig. 28: Fit of the theoretical model to the spectrum with $n = 30$ at high optical depth in the fiber with a core size of $60 \mu\text{m}$. The parameters for the theoretical curve are $T = 296 \text{ K}$, $w_0 = 19.2 \mu\text{m}$, $P_P = 0.2 \mu\text{W}$, $P_I = 2.4 \mu\text{W}$, $P_C = 201(8) \text{ mW}$, $amp = 1.71(4) \times 10^5$ and $V_{\text{fos}} = 580 \pm 53$.

decay of Rydberg states into levels not included in the simulation are assumed to contribute to an effective decay rate Γ_{41} . However, a decay into the second hyperfine level of the electronic ground state can not be covered by this rate. Adding one or more levels to the theory might help to model the system in a more realistic way.

9 Summary

In this work, the first successful excitation of Rydberg atoms from a thermal cloud of cesium atoms, confined inside hollow core fibers, has been demonstrated by a three photon excitation. Spectroscopic signals of Rydberg states with main quantum numbers between $n = 26$ and $n = 46$ have been observed. The experiments were performed in kagomé hollow core photonic crystal fibers with core diameters of $60\ \mu\text{m}$ and $19\ \mu\text{m}$ as well as in a capillary with a core diameter of $70\ \mu\text{m}$.

The diffusion of cesium atoms into the fibers was modeled with a simple diffusion equation including absorption and desorption of the atoms on the fiber walls. To do so, the diffusion coefficient had to be extended to include the sticking time. The simulations result in reasonable filling times, when compared to the experimental observations.

To investigate possible influences due to the fiber confinement, the three photon Rydberg spectra inside the fiber were compared to a reference signal recorded in a macroscopic vapor cell. For low main quantum numbers, the spectra measured in the kagomé HC-PCF with $60\ \mu\text{m}$ core diameter did not show any significant broadening and line shift in comparison to the reference spectrum. However, for higher main quantum numbers as well as for the smaller kagomé HC-PCF of $19\ \mu\text{m}$ core diameter, the signal revealed a broadening and a shifting of the lines. The frequency shifts, which were observed at low optical density after two months of exposure to the cesium atmosphere, might be addressed to external, disturbing electric fields. The line shifts vanished after the fibers were exposed to the cesium atmosphere for four months. During this larger exposure time also the optical depth in the system increased. While some residual broadening was still observable after four months of exposure in the $19\ \mu\text{m}$ core kagomé HC-PCF, the spectra taken in the kagomé HC-PCF with $60\ \mu\text{m}$ core diameter, did not exhibit a recognizable broadening anymore. Deviations for higher main quantum numbers as well as for smaller core diameters need to be investigated in future work, to understand to what extend Rydberg physics performed in vapor cells can be integrated into hollow core fibers.

The measurements performed in a capillary with $70\ \mu\text{m}$ core diameter were possible for Rydberg states with main quantum numbers up to $n = 46$. Here, no influences of the thicker core walls was observed, which is not surprising, considering the large core diameter. Future measurements on smaller capillaries could then unveil how atom wall interactions depend on the thickness of the core walls, by comparison between photonic crystal fibers and capillaries.

In a last step, the excitation of Rydberg atoms was demonstrated in a slightly different way, having the intermediate laser frequency stabilized off-resonantly. This

9 Summary

reduces the four level system effectively to a three level system, revealing the well known EIT features.

A model was developed to fit theoretical three photon absorption spectra to the experimental data. It includes the four energy levels as well as the three light fields and takes into account the spontaneous decay of the electronic states, the Doppler effect for the thermal atoms and the Gaussian intensity profile of the excitation beams. The model can in principle reproduce the line shape of the measured signals. However, for the coupling of the 7S and the Rydberg state the measured and the theoretical power values show strong deviations. Moreover, it is not possible to fit a whole data set of several main quantum numbers addressed in a consistent way. The model needs to be extended to sufficiently describe the system.

Light induced atomic desorption in the kagomé HC-PCF with 19 μm core size evoked by the laser at 790 nm wavelength was investigated. A change in the optical depth by up to two orders of magnitude was observed. It was found out that the change in the optical depth does not follow the switching of the LIAD beam immediately for frequencies higher than 100 Hz. The timescale suggests that the effect observed is surface-plasmon-induced desorption, where the excitation of plasmonic resonances leads to heating of cesium clusters on the core walls.

A Numbers used in the Simulation

Property	Value	Reference
Quantum defect Cs nP _{3/2}	$\delta_p = 3.5589599$	[25]
Decay rate 6P _{1/2} to 6S _{1/2}	$\Gamma_{21} = 2\pi \times 4.575 \text{ MHz}$	[35]
Decay rate 7S _{1/2} to 6S _{1/2} via 6P _{3/2}	$\Gamma_{31} = 2\pi \times 1.814 \text{ MHz}$	[47]
Decay rate 7S _{1/2} to 6P _{1/2}	$\Gamma_{32} = 2\pi \times 0.992 \text{ MHz}$	[47]
Transition dipole matrix element: 6S _{1/2} to 6P _{1/2} in Cs	$d_{895} = 3.1869ea_0$ $d_{895} = 2.702 \times 10^{-29} \text{ Cm}$	[35]
For π transition: $F = 3; m_F = 0 \rightarrow F' = 4; m_{F'} = 0$	$d_{F895} = 1/\sqrt{3} \times d_{895}$ $d_{F895} = 1.560 \times 10^{-29} \text{ Cm}$	[35] (prefactor)
Transition dipole matrix element: 6P _{1/2} to 7S _{1/2} in Cs	$d_{1359} = 4.236/\sqrt{2}ea_0$ $d_{1359} = 2.539 \times 10^{-29} \text{ Cm}$	[48]
For π transition: $F = 3; m_F = 0 \rightarrow F' = 4; m_{F'} = 0$	$d_{F1359} = 1/\sqrt{3} \times d_{1359}$ $d_{F1359} = 1.466 \times 10^{-29} \text{ Cm}$	[35] (prefactor)
Transition dipole matrix element: 7S _{1/2} to nP _{3/2} in Cs	$d_{\text{scal}} = 3.390ea_0(n - \delta_p)^{-3/2}$	internal wiki
With prefactor from Wigner symbols: for 7S _{1/2} to nP _{3/2}	$d_{\text{Ryd}} = 0.0786 d_{\text{scal}}$ $d_{\text{Ryd}(n=30)} = 1.661 \times 10^{-32} \text{ Cm}$	

B Wavelengths for the Rydberg transition

The wavelengths for the transitions from the cesium $7S_{1/2}$ state to the Rydberg states are given. In addition to the $nP_{3/2}$ Rydberg states, addressed in this work, the wavelengths for the $nP_{1/2}$ states are listed as well. Therefore, the energy of the $7S_{1/2}$ state, given in [49] was used and the energies levels for the Rydberg states were calculated, using the quantum defects given in [25].

n	Wavelength [nm] for	
	$7S_{1/2} \rightarrow nP_{1/2}$	$7S_{1/2} \rightarrow nP_{3/2}$
25	791.672	791.627
26	790.364	790.324
27	789.225	789.189
28	788.224	788.193
29	787.343	787.315
30	786.560	786.536
31	785.863	785.842
32	785.239	785.220
33	784.680	784.663
34	784.174	784.159
35	783.717	783.703
36	783.303	783.290
37	782.925	782.913
38	782.579	782.569
39	782.263	782.254
40	781.986	781.964
41	781.706	781.698
42	781.461	781.453
43	781.233	781.226
44	781.022	781.016
45	780.826	780.820
46	780.645	780.639
47	780.476	780.470
48	780.317	780.312
49	780.170	780.165
50	780.032	780.027
51	779.902	779.898
52	779.781	779.777
53	779.667	779.663
54	779.560	779.556
55	779.458	779.455
56	779.363	779.360
57	779.273	779.270
58	779.188	779.185
59	779.108	779.105
60	779.031	779.029

C Spectra Measured in Kagomé HC-PCF

To get a systematic dependence of the line shifts, observed in the kagomé HC-PCF series of measurements have been performed, varying the main quantum number of the excitation. The line shifts shown in figures 19 and 22, were extracted from the spectra shown in the following figures.

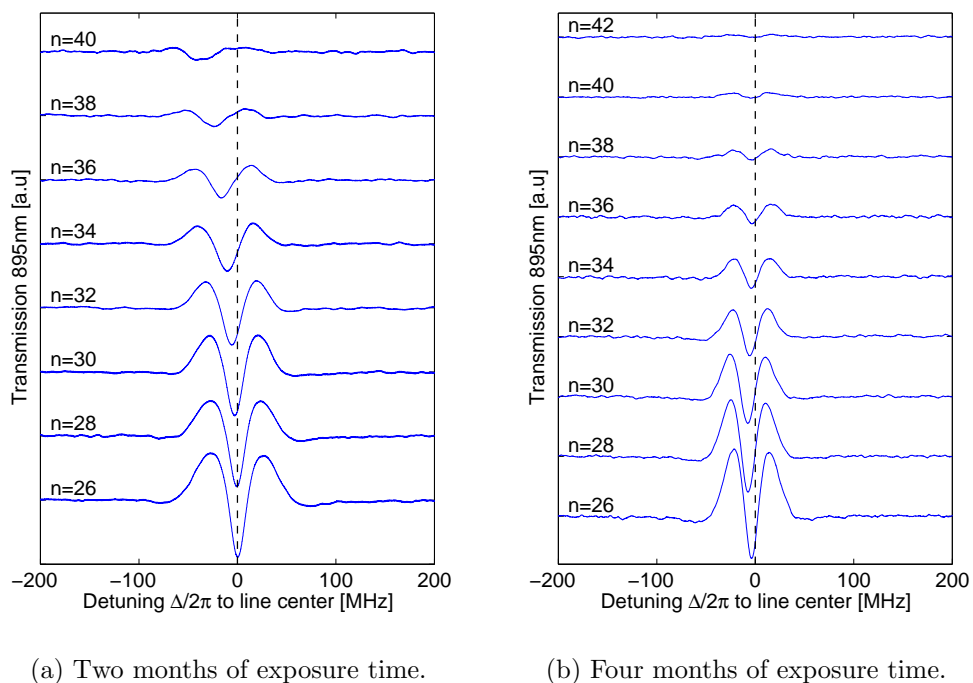


Fig. 29: Data sets of three photon signals in the kagomé HC-PCF with 60 μm core diameter with various main quantum numbers.

C Spectra Measured in Kagomé HC-PCF

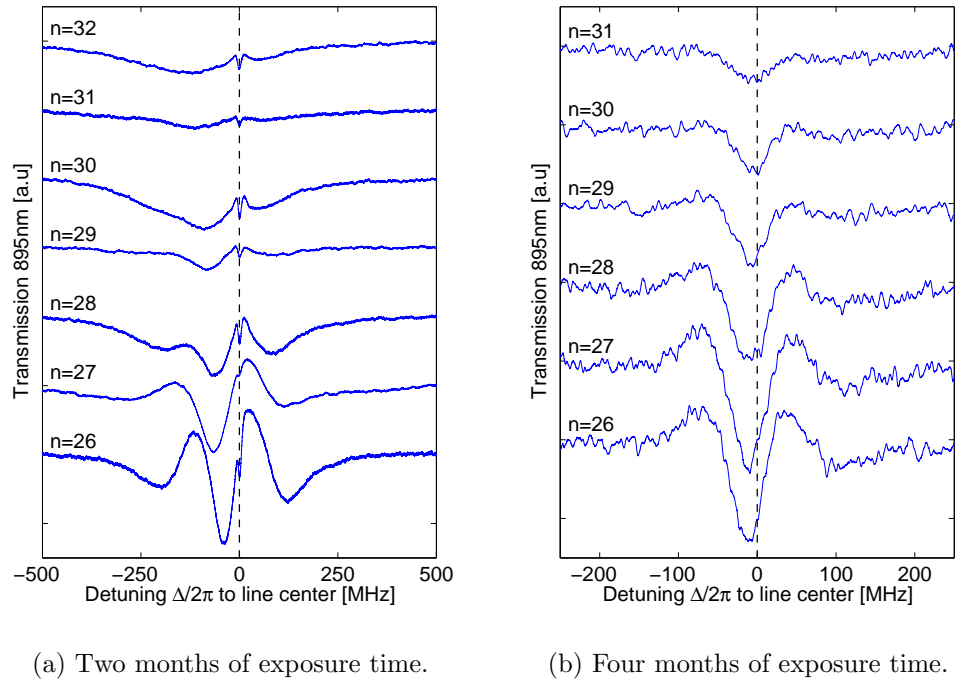


Fig. 30: Data sets of three photon signals in the kagomé HC-PCF with $19\ \mu\text{m}$ core diameter with various main quantum numbers.

Hiermit versichere ich, dass ich die Arbeit selbstständig verfasst habe, keine anderen als die angegebenen Quellen verwendet habe und alle wörtlich oder sinngemäß aus anderen Werken übernommenen Aussagen als solche gekennzeichnet habe. Weiterhin ist die eingereichte Arbeit weder vollständig noch in wesentlichen Teilen Gegenstand eines anderen Prüfungsverfahrens gewesen. Weder Teile der Arbeit noch die gesamte Arbeit wurden bisher veröffentlicht. Der Inhalt des elektronischen Exemplars stimmt mit dem des Druckexemplars überein.

Bibliography

- [1] C. S. Adams, K. J. Weatherill, and J. D. Pritchard. Nonlinear Optics using Cold Rydberg Atoms. *Annual Review of Cold Atoms and Molecules*, (8):301–350.
- [2] Y. O. Dudin and A. Kuzmich. Strongly Interacting Rydberg Excitations of a Cold Atomic Gas. *Science*, 336(6083):887–889, 2012.
- [3] T. Peyronel, O. Firstenberg, Q.-Y. Liang, S. Hofferberth, A. V. Gorshkov, T. Pohl, M. D. Lukin, and V. Vuletic. Quantum Nonlinear Optics with Single Photons Enabled by Strongly Interacting Atoms. *Nature*, 488(7409):57–60, AUG 2 2012.
- [4] L. Isenhower, E. Urban, X. L. Zhang, A. T. Gill, T. Henage, T. A. Johnson, T. G. Walker, and M. Saffman. Demonstration of a Neutral Atom Controlled-NOT Quantum Gate. *Physical Review Letters*, 104(1), JAN 8 2010.
- [5] T. Wilk, A. Gaetan, C. Evellin, J. Wolters, Y. Miroshnychenko, P. Grangier, and A. Browaeys. Entanglement of Two Individual Neutral Atoms using Rydberg Blockade. *Physical Review Letters*, 104(1), JAN 8 2010.
- [6] M. Saffman, T. G. Walker, and K. Molmer. Quantum Information with Rydberg Atoms. *Reviews of Modern Physics*, 82(3):2313–2363, AUG 18 2010.
- [7] H. Weimer, M. Mueller, I. Lesanovsky, P. Zoller, and H. P. Büchler. A Rydberg Quantum Simulator. *Nature Physics*, 6(5):382–388, MAY 2010.
- [8] H. Kuebler, J. P. Shaffer, T. Baluktsian, R. Loew, and T. Pfau. Coherent Excitation of Rydberg Atoms in Micrometre-Sized Atomic Vapour Cells. *Nature Photonics*, 4(2):112–116, FEB 2010.
- [9] T. Baluktsian, B. Huber, R. Löw, and T. Pfau. Evidence for Strong van der Waals Type Rydberg-Rydberg Interaction in a Thermal Vapor. *Phys. Rev. Lett.*, 110:123001, Mar 2013.
- [10] J. A. Sedlacek, A. Schwettmann, H. Kübler, R. Löw, T. Pfau, and J. P. Shaffer. Microwave Electrometry with Rydberg Atoms in A Vapour Cell using Bright Atomic Resonances. *Nature Physics*, 8:819–824, 2012.
- [11] P. St. J. Russell. Photonic Crystal Fibers. *Science*, 299(5605):358–362, 2003.

Bibliography

- [12] S. O. Konorov, A. B. Fedotov, and A. M. Zheltikov. Enhanced Four-Wave Mixing in A Hollow-Core Photonic-Crystal Fiber. *Optics Letters*, 28(16):1448–1450, AUG 15 2003.
- [13] P. S. Light, F. Benabid, F. Couny, M. Maric, and A. N. Luiten. Electromagnetically Induced Transparency in Rb-Filled Coated Hollow-Core Photonic Crystal Fiber. *Optics Letters*, 32(10):1323–1325, MAY 15 2007.
- [14] S. Ghosh, A. R. Bhagwat, C. K. Renshaw, S. Goh, A. L. Gaeta, and B. J. Kirby. Low-Light-Level Optical Interactions with Rubidium Vapor in A Photonic Band-Gap Fiber. *Physical Review Letters*, 97(2), JUL 14 2006.
- [15] P. Londero, V. Venkataraman, A. R. Bhagwat, A. D. Slepko, and A. L. Gaeta. Ultralow-Power Four-Wave Mixing with Rb in a Hollow-Core Photonic Band-Gap Fiber. *Physical Review Letters*, 103(4), JUL 24 2009.
- [16] F. Benabid, F. Couny, J. C. Knight, T. A. Birks, and P. St. J. Russell. Compact, Stable and Efficient All-Fibre Gas Cells using Hollow-Core Photonic Crystal Fibres. *Nature*, 434(7032):488–491, MAR 24 2005.
- [17] M. R. Sprague, D. G. England, A. Abdolvand, J. Nunn, X.-M. Jin, W. S. Kolthammer, M. Barbieri, B. Rigal, P. S. Michelberger, T. F. M. Champion, P. St. J. Russell, and I. A. Walmsley. Efficient Optical Pumping And High Optical Depth in A Hollow-Core Photonic-Crystal Fibre for A Broadband Quantum Memory. *New Journal of Physics*, 15(5):055013, 2013.
- [18] M. Bajcsy, S. Hofferberth, V. Balic, T. Peyronel, M. Hafezi, A. S. Zibrov, V. Vuletic, and M. D. Lukin. Efficient All-Optical Switching using Slow Light within a Hollow Fiber. *Physical Review Letters*, 102(20), MAY 22 2009.
- [19] T. G. Euser, G. Whyte, M. Scharrer, J. S. Y. Chen, A. Abdolvand, J. Nold, C. F. Kaminski, and P. St. J. Russell. Dynamic Control of Higher-Order Modes in Hollow-Core Photonic Crystal Fibers. *Optics Express*, 16(22):17972–17981, OCT 27 2008.
- [20] E. Shahmoon, G. Kurizki, M. Fleischhauer, and D. Petrosyan. Strongly Interacting Photons in Hollow-Core Waveguides. *Physical Review A*, 83(3), MAR 7 2011.
- [21] H. P. Breuer and F. Petruccione. *The Theory of Open Quantum Systems*. Oxford University Press, 2007.
- [22] C. Foot. *Atomic Physics*. Oxford University Press, 2004.
- [23] W. Demtröder. *Laser Spectroscopy Vol. 1*. Springer-Verlag, 2008.
- [24] M. Tanasittikosol. *Rydberg Dark States in External Fields*. PhD thesis, Durham University, UK, 2011.

- [25] C.-J. Lorenzen and K. Niemax. Precise Quantum Defects of nS, nP And nD Levels in Cs I. *Zeitschrift für Physik A Atoms and Nuclei*, 315(2):127–133, 1984.
- [26] R. Heidemann. *Rydberg Excitation of Bose-Einstein Condensates: Coherent Collective Dynamics*. PhD thesis, Universität Stuttgart, 2008.
- [27] S. Gu, S. Gong, B. Liu, J. Wang, Z. Dai, T. Lei, and B. Li. Experimental Study of Caesium Atom Rydberg State Polarizabilities by Doppler-Free Resonantly Enhanced Two-Photon Technique. *Journal of Physics B: Atomic, Molecular and Optical Physics*, 30(3):467, 1997.
- [28] F. K. Kneubühl and M. W. Sigrist. *Laser*. Vieweg + Teubner, Wiesbaden, 2008.
- [29] E.A.J Marcantili and R.A. Schmelzter. Hollow Metallic and Dielectric Waveguides for Long Distance Optical Transmission and Lasers. *Bell System Technical Journal*, 43(4P2):1783+, 1964.
- [30] R. K. Nubling and J. A. Harrington. Launch Conditions and Mode Coupling in Hollow-Glass Waveguides. *Optical Engineering*, 37(9):2454–2458, SEP 1998.
- [31] G. J. Pearce, G. S. Wiederhecker, C. G. Poulton, S. Burger, and P. St. J. Russell. Models for Guidance in Kagomé-Structured Hollow-Core Photonic Crystal Fibres. *Opt. Express*, 15(20):12680–12685, Oct 2007.
- [32] M. A. Finger, N. Y. Joly, T. Weiss, and P. St.J. Russell. Accuracy of the Capillary Approximation for Gas-Filled Kagomé-Style Photonic Crystal Fibers. *Opt. Lett.*, 39(4):821–824, Feb 2014.
- [33] A. Gozzini, F. Mango, J. H. Xu, G. Alzetta, F. Maccarrone, and R. A. Bernheim. Light-Induced Ejection of Alkali Atoms in Polysiloxane Coated Cells. *Nuovo Cimento Della Societa Italiana Di Fisica D-Condensed Matter Atomic*.
- [34] A. Burchianti, A. Bogi, C. Marinelli, C. Maibohm, E. Mariotti, and L. Moi. Reversible Light-Controlled formation And Evaporation of Rubidium Clusters in Nanoporous Silica. *Physical Review Letters*, 97(15), OCT 13 2006.
- [35] D. A. Steck. Cesium D Line Data, 2009.
- [36] C. Carr, C. S. Adams, and K. J. Weatherill. Polarization Spectroscopy of An Excited State Transition. *Optics Letters*, 37(1):118–120, Jan 1 2012.
- [37] P. Ilzhöfer. *Spektroskopie von thermischem Cäsium-Dampf in Hohlkernfasern*. Bachelor thesis, Universität Stuttgart, 2012.
- [38] L. Bauer. *Sättigungsspektroskopie in Cäsium-gefüllten Glaskapillaren*. Diploma thesis, Universität Stuttgart, 2012.

Bibliography

- [39] W. Demtröder. *Experimentalphysik 1*. Springer-Verlag, 2013.
- [40] WebElements: the Periodic Table On the Web, 08.04.2014.
- [41] P Clausing. Über die Adsorptionszeit und ihre Messung durch Strömungsversuche. *Annalen der Physik*, 7(4):489–520, NOV 1930.
- [42] J.H. de Boer. *The Dynamical Character of Adsorption*. Oxford University Press, 1968.
- [43] MA Bouchiat, J Guena, P Jacquier, M Lintz, and AV Papoyan. Electrical Conductivity of Glass and Sapphire Cells Exposed To Dry Cesium Vapor. *Applied Physics B-Lasers and Optics*, 68(6):1109–1116, JUN 1999.
- [44] C Marinelli, KA Nasyrov, S Bocci, B Pieragnoli, A Burchianti, V Biancalana, E Mariotti, SN Atutov, and L Moi. A New Class of Photo-Induced Phenomena in Siloxane Films. *European Physical Journal D*, 13(2):231–235, FEB 2001.
- [45] A. R. Bhagwat, A. D. Slepko, V. Venkataraman, P. Londero, and A. L. Gaeta. On-Demand All-Optical Generation of Controlled Rb-Vapor Densities in Photonic-Band-Gap Fibers. *Phys. Rev. A*, 79:063809, Jun 2009.
- [46] C. Carr, M. Tanasittikosol, A. Sargsyan, D. Sarkisyan, C. S. Adams, and K. J. Weatherill. Three-Photon Electromagnetically Induced Transparency using Rydberg States. *Opt. Lett.*, 37(18):3858–3860, Sep 2012.
- [47] O.S. Heavens. Radiative Transition Probabilities of Lower Excited States of Alkali Metals. *Journal of the Optical Society of America*, 51(10):1058–&, 1961.
- [48] AA Vasilyev, IM Savukov, MS Safronova, and HG Berry. Measurement of the 6s-7p Transition Probabilities in Atomic Cesium and a Revised Value for the Weak Charge Q(W). *Physical Review A*, 66(2), AUG 2002.
- [49] J. E. Sansonetti. Wavelengths, Transition Probabilities, and Energy Levels for the Spectra of Cesium (Cs I-Cs LV). *Journal of Physical and Chemical Reference Data*, 38(4):761–923, DEC 2009.